JOURNAL OF GEOPHYSICAL RESEARCH, VOL. 110, B07301, doi:10.1029/2004JB003524, 2005

Source mechanism of Vulcanian degassing at Popocatépetl Volcano, Mexico, determined from waveform inversions of very long period signals

Bernard Chouet and Phillip Dawson
U.S. Geological Survey, Menlo Park, California, USA

Alejandra Arciniega-Ceballos
Instituto de Geofisica, Universidad Nacional Autónoma de México, México City, Mexico

Received 4 November 2004; revised 2 March 2005; accepted 15 March 2005; published 6 July 2005.

[1] The source mechanism of very long period (VLP) signals accompanying volcanic degassing bursts at Popocatépetl is analyzed in the 15–70 s band by minimizing the residual error between data and synthetics calculated for a point source embedded in a homogeneous medium. The waveforms of two eruptions (23 April and 23 May 2000) representative of mild Vulcanian activity are well reproduced by our inversion, which takes into account volcano topography. The source centroid is positioned 1500 m below the western perimeter of the summit crater, and the modeled source is composed of a shallow dipping crack (sill with easterly dip of 10°) intersecting a steeply dipping crack (northeast striking dike dipping 83° northwest), whose surface extension bisects the vent. Both cracks undergo a similar sequence of inflation, deflation, and reinflation, reflecting a cycle of pressurization, depressurization, and repressurization within a time interval of 3–5 min. The largest moment release occurs in the sill, showing a maximum volume change of 500–1000 m^3, pressure drop of 3–5 MPa, and amplitude of recovered pressure equal to 1.2 times the amplitude of the pressure drop. In contrast, the maximum volume change in the dike is less (200–300 m^3), with a corresponding pressure drop of 1–2 MPa and pressure recovery equal to the pressure drop. Accompanying these volumetric sources are single-force components with magnitudes of 10^8 N, consistent with melt advection in response to pressure transients. The source time histories of the volumetric components of the source indicate that significant mass movement starts within the sill and triggers a mass movement response in the dike within a few seconds. Such source behavior is consistent with the opening of a pathway for escape of pent-up gases from slow pressurization of the sill driven by magma crystallization. The opening of this pathway and associated rapid evacuation of volcanic gases induces the pressure drop. Pressure recovery in the magma filling the sill is driven by diffusion of gases from the resulting supersaturated melt into bubbles. Assuming a penny-shaped crack at ambient pressure of 40 MPa, the observed pressure and volume variations can be modeled with the following attributes: crack radius (100 m), crack aperture (5 m), bubble number density (10^{10}–10^{12} m^{-3}), initial bubble radius (10^{-6} m), final bubble radius ($\sim 10^{-5}$ m), and net decrease of gas concentration in the melt (0.01 wt %).

Citation: Chouet, B., P. Dawson, and A. Arciniega-Ceballos (2005), Source mechanism of Vulcanian degassing at Popocatépetl Volcano, Mexico, determined from waveform inversions of very long period signals, *J. Geophys. Res.*, *110*, B07301, doi:10.1029/2004JB003524.

1. Introduction

[2] Popocatépetl Volcano is a large, glacier-clad, 5452 m high composite volcano, located 60 km southeast of Mexico City in the central region of the Trans-Mexican Volcanic Belt. Its last major Plinian eruption occurred circa 822–823 A.D. [*Siebe et al.*, 1996]. During the past 70 years, volcanic activity was limited to mild fumarolic emissions through vents in the crater. Then the fumarolic activity began to increase in 1993, heralding renewed unrest. Seismic activity, initially monitored with a single three-component short-period (1 Hz) seismometer located 5 km north of the crater (station PPIG in Figure 1), significantly increased in October 1994. A swarm of volcano-tectonic (VT) earthquakes, followed by sustained tremor accompa-

0148-0227/05/2004JB003524$09.00

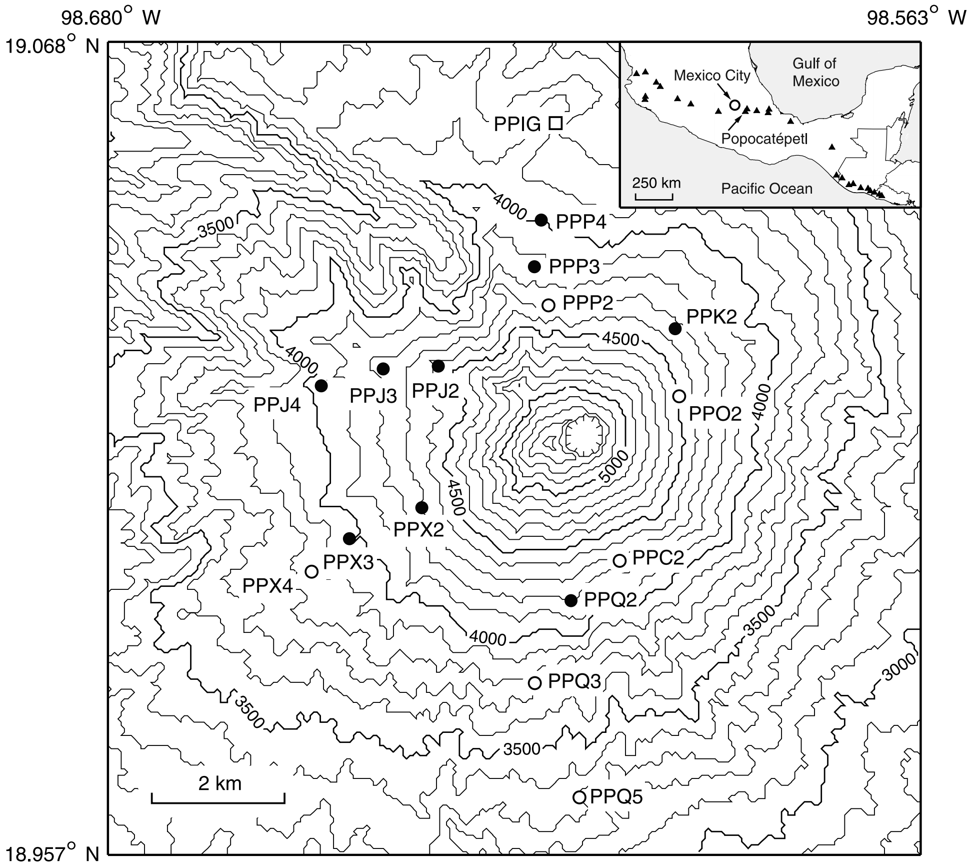

Figure 1. Map of summit area of Popocatépetl Volcano showing locations of three-component broadband stations (solid dots) used in our experiment. Stations indicated by open circles were inoperative during the time of this study. Station PPIG (open square) is a permanent station of the national seismic network. Contours represent 100 m elevation intervals. The inset shows the location of Popocatépetl among volcanoes (triangles) of the Trans-Mexican Volcanic Belt.

nying a large ash plume, marked the reawakening of Popocatépetl on 21 December 1994 [*Arciniega-Ceballos et al.*, 2000]. This renewal of activity launched a program of systematic volcano monitoring [*Comité Cientifico Asesor CENAPRED-UNAM*, 1995; *Love et al.*, 1998; *Goff et al.*, 1998] and the rapid preparation of a volcanic hazards assessment and hazards zonation map [*Macias et al.*, 1995].

[3] Since December 1994, eruptive activity at Popocatépetl has been dominated by passive fumarolic emissions, interrupted by episodic more energetic emissions of ash and gas through vents in the summit crater, and dome formation and destruction within the crater. In late March 1996, a lava dome was first observed in the crater. This dome was partially destroyed on 30 April 1996, when a large eruption initiated a long phase of repetitive dome-building and dome-destroying episodes that continued through March 1999 [*Arciniega-Ceballos et al.*, 2003]. Activity remained limited to emissions of ash and gas and intermittent lava effusions during the next twenty months, following which explosive activity resumed with a large dome-destroying event on 17 December 2000. Dome formation and dome destruction activities persist to the present.

[4] The most common eruptive activity involves the emissions of ash-laden gases. These exhalations range in intensity from small, short-lived puffs, which may rise a few hundred meters above the crater rim, to larger plumes that may reach up to 5 km above the crater and blanket the entire summit area lightly with ash. Of note is the persistent low activity of VT earthquakes contrasting the high rates of long-period (LP) event production accompanying eruptive activity [*Arciniega-Ceballos et al.*, 2003]. LP events and tremor episodes at Popocatépetl are usually characterized by very emergent onsets and correlate in time with degassing and with the emplacement of lava domes. Very long period (VLP) signals have also been observed to systematically accompany ash emissions and Vulcanian explosions, consistent with the broadband character of the seismicity accompanying degassing activity at Popocatépetl [*Arciniega-Ceballos et al.*, 1999; *Cruz-Atienza et al.*, 2001; *Arciniega-Ceballos et al.*, 2003].

[5] Broadband observations of VLP seismicity associated with volcanic activity are not new, and examples from many volcanoes around the world point to the ubiquitous nature of these signals under a variety of volcanic conditions [*Kawakatsu et al.*, 1992, 1994; *Neuberg et al.*, 1994; *Uhira and Takeo*, 1994; *Kaneshima et al.*, 1996; *Ohminato and Ereditato*, 1997; *Ohminato et al.*, 1998; *Dawson et al.*, 1998; *Rowe et al.*, 1998; *Chouet et al.*, 1999; *Kawakatsu et al.*, 2000; *Legrand et al.*, 2000; *Nishimura et al.*, 2000; *Kumagai et al.*, 2001; *Hill et al.*, 2002; *Tameguri et al.*,

2002; *Hidayat et al.*, 2002; *Chouet et al.*, 2003; *Aster et al.*, 2003]. There are, however, relatively few published studies of source mechanism of volcanic activity based on systematic inversions of VLP waveforms [*Ohminato et al.*, 1998; *Nishimura et al.*, 2000; *Kumagai et al.*, 2001; *Chouet et al.*, 2003], and apart from limited investigations by *Uhira and Takeo* [1994] and *Tameguri et al.* [2002], no such studies have yet been made to shed light on the fundamental mechanisms underlying Vulcanian activity. The proximity of Popocatépetl to Mexico City and other populated areas underscores the need for a better understanding of the source processes of eruptive activity and associated hazards at this volcano [*Macias et al.*, 1995; *Siebe and Macias*, 2004]. Accordingly, detailed broadband measurements were obtained at Popocatépetl for about six months starting in November 1999 with the specific objective to elucidate the source mechanism and mass transport phenomena associated with Vulcanian eruptions.

[6] In this paper, we use the linear inversion method of *Ohminato et al.* [1998] to quantify the source mechanism of VLP waveforms observed during these eruptions. Synthetic waveforms are constructed by a superposition of impulse responses obtained for six moment tensor components and three single-force components applied at a point source embedded in the three-dimensional (3-D) edifice of Popocatépetl. We begin with a brief description of the broadband network and data recorded during the experiment, and proceed with an application of the inversion method to these data. We follow with a discussion of the implications of the source mechanism for the conduit geometry at Popocatépetl and transport dynamics associated with its Vulcanian eruptions.

2. Broadband Seismic Network

[7] Our data were recorded by a network of 15 three-component broadband seismometers (see Figure 1). The receiver layout was selected to provide homogeneous coverage in both azimuth and distance for sources located in the top 2 km of edifice below the summit crater. The network features: (1) a ring of seven sensors surrounding the edifice at elevations between 4200 and 4500 m and ranging in distance between 1.6 and 2.4 km from the active crater and (2) eight sensors distributed along four profiles extending northward, westward, southwestward, and southward from the summit, at elevations between 3300 and 4200 m, and distances ranging between 2.6 and 5.4 km from the crater. Sites for seismic sensor installation in the summit area of Popocatépetl were significantly limited by difficulties of access and logistics involved in station maintenance. Eleven sites were equipped with Guralp CMG-3ESP (0.02–100 s) seismometers, three featured Guralp CMG-3T (0.02–100 s) seismometers, and one featured a Strekeisen STS-2 (0.02–120 s) sensor. Data were recorded by 11 Guralp Storage Acquisition Module (SAM), 32-bit digital recorders, 3 Nanometrics Orion, 24-bit recorders, and 1 Reftek, 24-bit recorder, each operating in continuous mode at 100 samples s^{-1} $\mathrm{channel}^{-1}$. All the data loggers used a Global Positioning System (GPS) time base with an accuracy of 5 μs.

[8] All the receivers were positioned with GPS with an accuracy of 5 cm in absolute location. The orientation of horizontal components was obtained by field measurements with compass and are resolved with a precision of 5°. The entire network operated from 26 November 1999 through 31 March 2000. Starting on 1 April 2000, however, operation became limited to seven to nine stations owing to difficulties in performing regular scheduled maintenance of receivers located at the highest and lowest elevations on the edifice. The reduced network remained operational through 15 June 2000.

[9] Station PPIG, located at Cerro Tlamacas 5 km north of the crater, is a permanent station of the Servicio Sismológico Nacional, Instituto de Geofisica, UNAM. It features a three-component short-period (L-4C) seismometer, and broadband Strekeisen STS-2 sensor. Data from the latter sensor are recorded both in continuous mode at 1 sps and in trigger mode at 80 sps. These data are not included in our analyses because of the weakness of the VLP signals recorded at this distance during the operational period of our network.

3. Data

[10] Volcanic activity during the course of our experiment was dominated by episodic emissions of gas and ash, and by the formation of a lava dome within the summit crater. Bursts of volcanic degassing (“exhalations”) were accompanied by LP events observed as isolated events, or as sequences of discrete events with overall durations comparable to those of visible activity documented by video. Some gas emissions were accompanied by persistent or spasmodic tremor. LP events and tremor episodes increased in frequency and intensity in mid-February 2000 and remained at heightened levels of production through late April 2000. A small lava dome was visually observed in the summit crater during a helicopter flight on 25 February (CENAPRED Web site, http://www.cenapred.unam.mx/mvolcan.html). Swarms of hybrid events were also frequently observed during the 3 month interval February-April, suggesting that active dome growth was occurring throughout this interval.

[11] VLP signals accompanying exhalations were also clearly recorded at stations closest to the crater. Longer-lasting, mild Vulcanian eruptions were observed on three occasions in April-May 2000, each accompanied by bursts of tremor and significant energy in the LP and VLP bands (Figure 2). For comparison, the VLP signal associated with an exhalation on 4 February 2000 is also displayed in Figure 2. The VLP signals are obtained by low-pass filtering the data below 15 s with a two-pole zero-phase shift Butterworth filter and faithfully reproduce the VLP components present in the broadband data.

[12] The VLP waveforms of exhalation signals recorded by our network all display a similar compression-dilatation-compression displacement sequence as exemplified by the event on 4 February illustrated in Figure 2. This similarity among VLP waveforms from different events clearly reflects the repetitive action of a nondestructive source. The broadband seismograms of individual exhalations are generally emergent and have typical durations of 1–3 min, roughly comparable to the overall duration of the main VLP signal. In contrast, the broadband signatures of the eruptions in Figure 2 last 30–80 min, and within this time interval

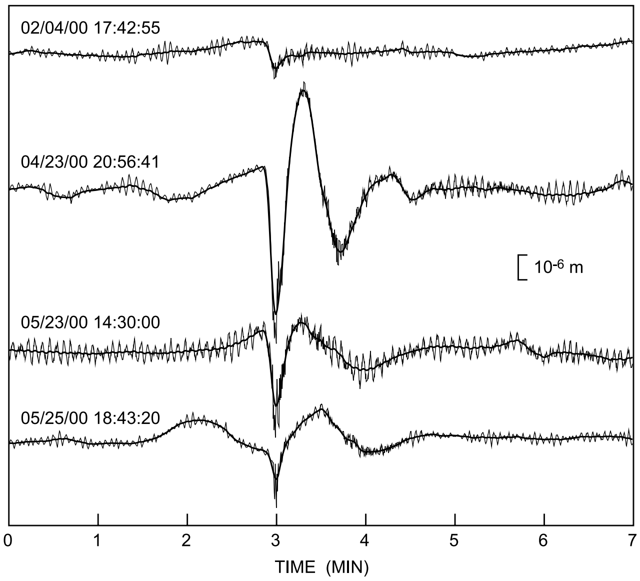

Figure 2. Vertical displacements recorded at station PPQ2 for one exhalation (top trace) and three eruptions (bottom three traces) at Popocatépetl. A filtered record (thick line) overlaid on the actual broadband record (thin line) is shown for each event. The date and time at the start of each record are indicated at the top left of the record. These data are representative of true ground motion after deconvolution for instrument response.

significant VLP energy release is limited to approximately the first 6 min in the 23 April and 25 May eruptions, or 6 min starting 24 min after the onset of the broadband signal in the 23 May eruption. Weak VLP signals are observed only at station PPQ2 during the remainder of these eruptions. Although the VLP waveforms for the Vulcanian eruptions in April and May differ from those of exhalations in the characteristics of recovery following the main dilatational pulse, their onsets are similar to those displayed by exhalations. These features are especially obvious in the two eruptions on 23 April and 23 May, which both display VLP signals marked by an initial compressional ramp lasting approximately 1 min, interrupted by a strong dilatational pulse as in the exhalation waveform.

[13] A repetitive nondestructive source process is further evidenced by particle motions observed at receivers near the summit of Popocatépetl for these events. Figure 3 shows particle motions obtained in the 15–70 s band for the two eruptions on 23 April and 23 May. Horizontal and vertical particle motions all consistently point to a small region located below the summit crater. Particle motions recorded for the exhalation on 4 February and eruption on 25 May are similar to those recorded for the more energetic eruptions in April and May (Figure 4). On the basis of our observation that all the VLP waveforms in exhalations and eruptions have similar characteristics, we infer that the operative source processes are essentially stationary with time within the bandwidth of our VLP data; thus an analysis of representative events is adequate to fully describe the overall source dynamics.

[14] Seismic signals associated with volcanic activity are not accessible at periods overlapping the typical 3–10 s band of oceanic noise at Popocatépetl [*Arciniega-Ceballos et al.*, 1999]. To avoid contamination by this source of noise, our analyses of VLP signals are restricted to periods longer than 15 s. Furthermore, the signal-to-noise ratios are weak and unreliable at periods longer than 70 s. To lessen data contamination due to increased sensitivity to noise at periods longer than 70 s, we high pass the waveforms at 70 s. VLP signals from exhalations are weaker than those recorded during eruptions (see Figure 2), generally resulting in poor signal-to-noise ratios at most receivers. Accordingly, we restrict our analyses to the two strongest events recorded (23 April

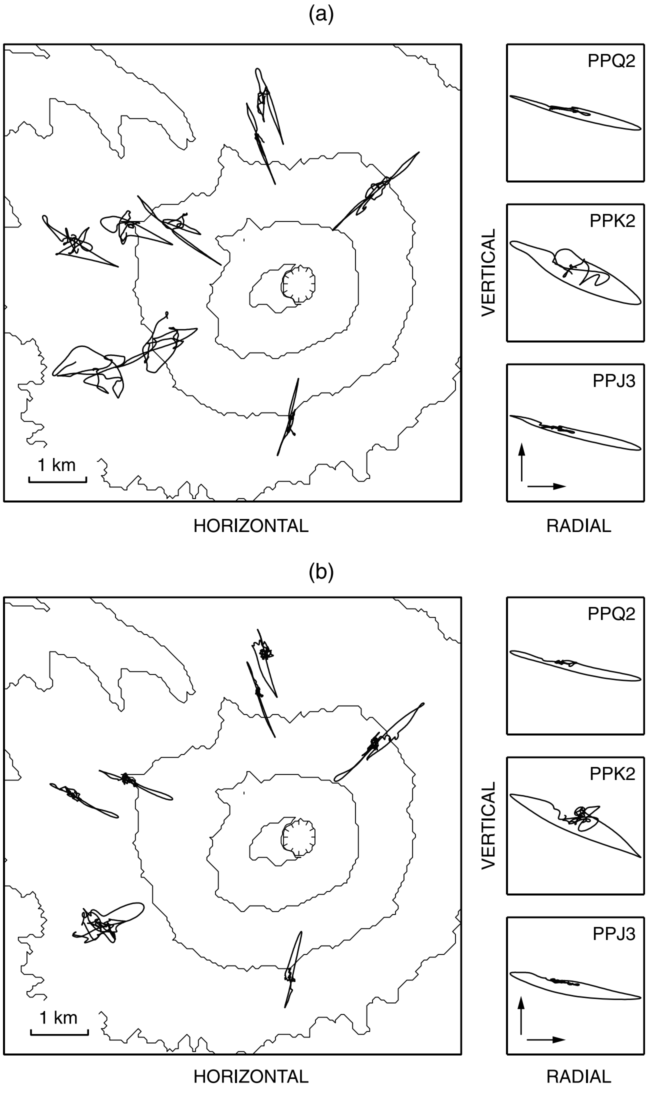

Figure 3. Normalized particle velocities observed on the network. These represent data deconvolved for instrument response and band-pass filtered in the 15–70 s band using a two-pole zero-phase-shift Butterworth filter. (a) Particle trajectories in the (left) horizontal and (right) vertical radial planes for the 23 April event. The positive radial direction in the vertical-radial plane points to the source (see arrows in plot at bottom right). (b) The same as Figure 3a for the 23 May event.

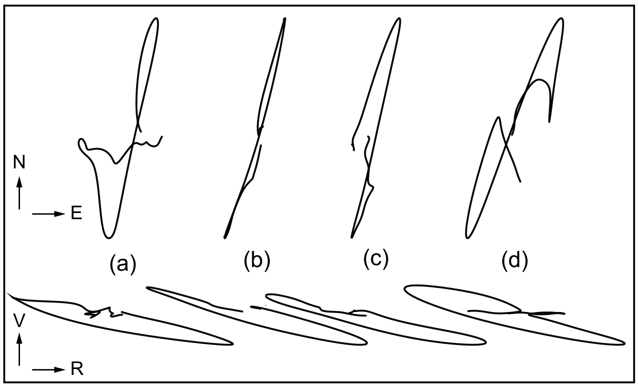

Figure 4. Comparison of normalized particle velocities in the (top) horizontal and (bottom) vertical radial planes recorded at station PPQ2 for the four events in Figure 2. These are deconvolved data band-pass filtered with the same filter as in Figure 3. The data are as follows: a, 4 February exhalation; b, 23 April eruption; c, 23 May eruption; d, 25 May eruption.

and 23 May) to quantify the source mechanisms representative of degassing at Popocatépetl.

4. Data Analysis and Results

4.1. Inversion Method

[15] The displacement field generated by a seismic source is described by the representation theorem which, for a point source, may be written as [*Chouet*, 1996, equation 8]

$$u_n(t) = F_p(t) * G_{np}(t) + M_{pq}(t) * G_{np,q}(t), \quad p, q = x, y, z, \tag{1}$$

where $u_n(t)$ is the n component of seismic displacement at a receiver at time t, $F_p(t)$ is the time history of the force applied in the p direction, $M_{pq}(t)$ is the time history of the pq component of the moment tensor, and $G_{np}(t)$ is the Green tensor which relates the n component of displacement at the receiver position with the p component of impulsive force at the source position. The notation $,q$ indicates spatial differentiation with respect to the q coordinate and the asterisk denotes convolution. Summation over repeated indices is implied.

[16] To invert our data with equation (1), we follow *Ohminato et al.* [1998] and *Chouet et al.* [2003]. In this approach, the source location is fixed, and the unknown source time functions for moment tensor and single-force components are represented by series of regularly spaced elementary functions (given by equation (4) in section 4.2), each with a different amplitude and sign. Equation (1) may be written in matrix form

$$\mathbf{d} = \mathbf{Gm}, \tag{2}$$

in which **d** represents the data vector, **G** is the matrix of Green's functions, and **m** is the vector containing the unknown source time functions. Minimization of the square of the residual vector between data and synthetics in (2) then yields the solution

$$\mathbf{m} = (\mathbf{G}^t\mathbf{G})^{-1}\mathbf{G}^t\mathbf{d}, \tag{3}$$

where $\mathbf{G}^t$ is the transpose of matrix **G**. In this equation, **m** has dimensions $N_m N_\tau$, **d** has dimensions $N_t N_s$, and **G** has dimensions $N_t N_s$ by $N_m N_\tau$, where N_m is the number of source mechanism components, N_t is the number of observed seismic traces, N_s is the number of samples in each trace, and N_τ is the number of elementary functions used to represent the source time function. The source location is fixed, and the amplitudes of all the elementary source pulses are determined simultaneously from the set of linear equations (3). In this manner, each sample of each source time function in the distribution of force and/or moment at the source is obtained independently. In our inversion of data from Popocatépetl, we conduct a grid search with respect to source location and determine the best solution for a single point source.

4.2. Calculation of Green's Functions

[17] Our calculations of Green's functions assume a homogeneous medium and include the topography of Popocatépetl. On the basis of the structural data elaborated by *Valdes et al.* [1995], we assume a compressional wave velocity V_p = 3.5 km/s, shear wave velocity V_s = 2 km/s, and density ρ = 2650 kg/m^3. Wavelengths corresponding to the period range 15–70 s of the observed signals span 30–250 km so that small-scale velocity heterogeneities are assumed to have negligible effect on our results. Green's functions are convolved with a smoothing function to insure the stability of the inversion. We use the cosine smoothing function

$$S(t) = \begin{cases} \dfrac{1}{2}\left[1 - \cos\left(\dfrac{2\pi t}{t_p}\right)\right], & 0 \le t \le t_p, \\ 0, & t > t_p, \end{cases} \tag{4}$$

in which t_p = 4.0 s. The smoothed cosine function convolved with the Green's functions represents our elementary source time function, and the true source time function is obtained by a superposition of these elementary functions. No anelastic attenuation is included in our calculations of Green's functions, because all receivers in the Popocatépetl network are located within a fraction of wavelength from the source, and anelastic attenuation effects are negligible over such short distances.

[18] Synthetics are obtained by the three-dimensional finite difference method of *Ohminato and Chouet* [1997], in which the topography of Popocatépetl is discretized in a staircase by stacking unit cells with fixed cell size. The computational domain is centered on the edifice and has lateral dimensions of 16.25 × 16.25 km, and vertical extent of 11 km (Figure 5). Our calculations are performed over a grid of 50 × 50 × 50 m, yielding a 3-D mesh with 326 × 326 × 221 nodes. The grid size considered is small enough to satisfy the criterion of minimum number of grids per wavelength established by *Ohminato and Chouet* [1997], and the size of the computational domain is sufficiently large to minimize spurious edge reflections, yet small

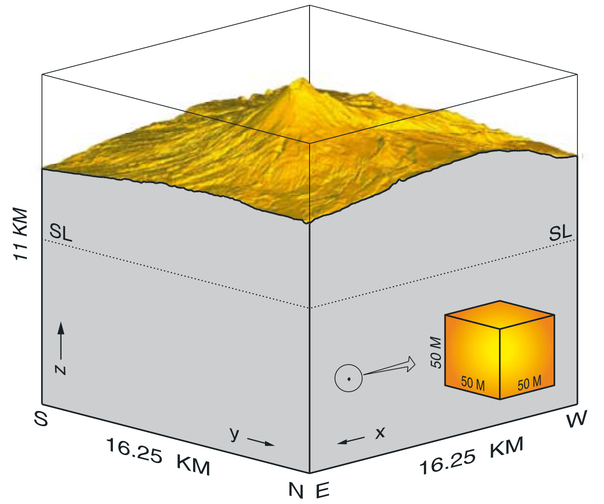

Figure 5. Extent of domain and grid size selected for finite difference calculations for Popocatépetl Volcano (see text for details). Sea level (SL) is indicated by the dotted line.

enough to preclude prohibitive calculations. The Cartesian coordinates are set with origin at the bottom southwest corner of the domain, with *x* axis positive eastward, *y* axis positive northward, and *z* axis positive upward. The top boundary of the domain is set to coincide with the top of Popocatépetl at an altitude of 5452 m. The topography of Popocatépetl is obtained from a digital elevation map (DEM) provided by the Instituto Nacional de Estadistica, Geográfia e Informática (INEGI) of Mexico.

[19] The search for the best fit point source is conducted for point sources distributed in a 3-D mesh extending below the summit crater. The domain considered includes a core of densely distributed nodes surrounded by a coarser distribution of nodes. In the core region, centered beneath the crater, point sources are positioned at individual grid nodes spaced 50 m apart in a uniform mesh extending 750 m in the east-west and 500 m in the north-south directions, and from 3200 to 3850 m in elevation. In the surrounding region, point sources are spaced 100 m apart in a uniform mesh extending over 1000 m in the east-west and north-south directions and from 3150 to 5050 m in elevation. The total number of point sources involved is 4134.

[20] As the number of point sources investigated is quite large, we make use of the reciprocity theorem [*Aki and Richards*, 1980]. The reciprocal relation between source and receiver is expressed as

$$G_{mn}(\mathbf{x}_1, \mathbf{x}_2) = G_{nm}(\mathbf{x}_2, \mathbf{x}_1), \qquad (5)$$

where $G_{mn}(\mathbf{x}_1, \mathbf{x}_2)$ is the *m* component of displacement at $\mathbf{x}_1$ due to a unit impulse applied in the *n* direction at $\mathbf{x}_2$. Reciprocity states that the *m* component of displacement at $\mathbf{x}_1$ generated by a unit impulse applied in the *n* direction at $\mathbf{x}_2$ is the same as the *n* component of displacement at $\mathbf{x}_2$ due to a unit impulse applied in the *m* direction at $\mathbf{x}_1$. Using reciprocity, we calculate the three components of displacement at each source node generated by impulsive forces applied in the *x*, *y*, and *z* directions at each receiver location in the network. For the 15 three-component receivers, 45 computer runs are required to generate the required Green's functions for all the point sources in the source grid. Without the use of reciprocity, the number of runs required to generate the required set of Green's functions is more than 2 orders of magnitude larger. Use of reciprocity therefore amounts to a very significant saving in computational time.

[21] We tested the reciprocity theorem by comparing the Green's functions calculated by reciprocity with the Green's functions computed by the forward method. An example of results obtained by the two methods is shown in Figure 6, in which the waveforms calculated by the two different approaches are found to match each other precisely over the main portion of the Green's functions, but display small amplitude and phase discrepancies in the tail of the Green's functions. In these later portions of the Green's functions, the waveforms are contaminated by weak artificial reflections from the edges of the computational domain due the use of approximate absorbing boundary conditions [*Ohminato and Chouet*, 1997]. Thus the homogeneous boundary condition required by the reciprocity theorem is not perfectly satisfied by the artificial absorbing conditions used by *Ohminato and Chouet* [1997], and slight discrepancies appear in the two solutions as a result. Such discrepancies could be further reduced by the selection of a larger computation domain, but at the expense of a significant increase in computational time. Owing to their small amplitude and occurrence limited to the latter, low-amplitude portions of the Green's functions, these discrepancies were found to have insignificant effects on the results of our waveform inversions; thus we deemed the use of a larger computation domain was unnecessary.

4.3. Evaluation of Results

[22] Our inversions for best fit point source location consider three possible source mechanisms: (1) three

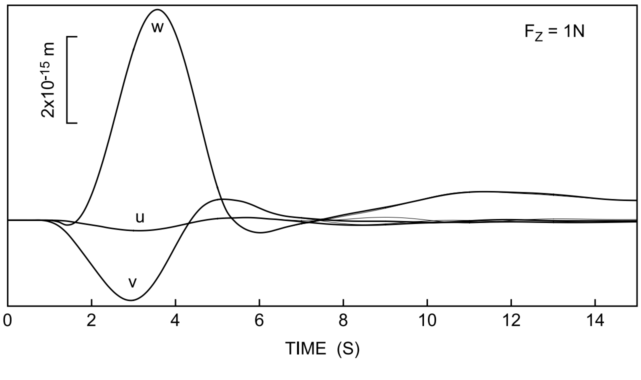

Figure 6. Comparison of Green's functions obtained by the forward (thick lines) and reciprocal (thin lines) methods. The three components of displacement, *u* (east), *v* (north), and *w* (up), are obtained at station PPQ2 for a single upward directed force with amplitude 1 N applied at a point centered 1.5 km below the summit crater floor (see Figure 1). The source time function of the force is a full cycle cosine with period t_p = 4 s (equation (4)). Over the main portion of the signals the match between the forward and reciprocal solutions is so good that the thin line curves are entirely beneath the thick lines, i.e., nearly all the differences are too small to be visible at the scale of the illustration.

single-force components only, (2) six moment tensor components only, and (3) six moment tensor components and three single-force components. The selection of an optimum solution is based on variance reduction, relevance of the free parameters used in the model, and physical significance of the resulting source mechanism. We use two definitions of squared error to evaluate the accuracy of our fits between synthetics and data [*Ohminato et al.*, 1998; *Chouet et al.*, 2003]

$$E_1 = \frac{\sum_{n=1}^{N_t}\sum_{p=1}^{N_s}\left(u_n^0(p\Delta t) - u_n^s(p\Delta t)\right)^2}{\sum_{n=1}^{N_t}\sum_{p=1}^{N_s}\left(u_n^0(p\Delta t)\right)^2} \times 100, \qquad (6)$$

and

$$E_2 = \frac{1}{N_r}\sum_{n=1}^{N_r}\left[\frac{\sum_{1}^{3}\sum_{p=1}^{N_s}\left(u_n^0(p\Delta t) - u_n^s(p\Delta t)\right)^2}{\sum_{1}^{3}\sum_{p=1}^{N_s}\left(u_n^0(p\Delta t)\right)^2}\right] \times 100, \qquad (7)$$

where $u_n^0(p\Delta t)$ is the pth sample of the nth data trace, $u_n^s(p\Delta t)$ is the pth sample of the nth synthetic trace, N_t is the number of data traces, N_s is the number of samples in each trace, and N_r is the number of three-component receivers. In equation (6), large-amplitude traces dominate the squared error, and the squared error remains small even when mismatches are present between data and synthetics for stations with weak amplitude signals, as long as the stations with large-amplitude signals are well matched by the synthetics. In equation (7), the squared error is normalized station-by-station, so that stations with weak amplitude signals contribute equally to the squared error as stations with large-amplitude signals.

[23] To test the significance of the number of free parameters each source model is evaluated by calculating Akaike's information criterion (AIC) [*Akaike*, 1974] defined as

$$\mathrm{AIC} = N_t N_s \ln E + 2 N_m N_\tau, \qquad (8)$$

in which the constant term is omitted. The parameter E in this equation represents the squared error defined according to equation (6) or (7). Additional free parameters in the source mechanism are considered to be physically relevant when both the residual error and AIC are minimized. A final test considers the physical relevance of the solution itself. A moment tensor solution is deemed relevant only if consistent waveform shapes are obtained among individual moment tensor components. This condition is necessary for a plausible interpretation of the source mechanism.

4.4. Results

[24] Figure 7 shows the distribution of residual errors E_2 obtained with equation (7) for the eruption on 23 May, the best resolved event in our data set. The error is representative of fits obtained for a source mechanism consisting of six moment tensor and three single-force components. The error minimum (E_2 = 7.8%, Table 1) yields a source centroid located at an elevation of 3600 m, approximately 1500 m below the western perimeter of the crater floor. Horizontal and vertical cross sections through the centroid provide measures of the spatial resolution of the centroid. Considering the error surface defined by an error increment of 0.5% above the minimum error as reference (see contours for E_2 = 8.3% in Figure 7), one obtains estimates of the spatial resolution of the centroid of ±300 m in the vertical direction, and $^{+400}_{-300}$ m and ±200 m in the east-west and north-south directions, respectively. The centroid location obtained according to the error estimate E_1 given by equation (6) falls slightly shallower and at the eastern edge of the error domain shown in Figure 7. The spatial resolution of this latter centroid is similar to that achieved with the error estimate E_2 (see Figure 7).

[25] Figure 8 shows the waveform match obtained by inversion of the data for the eruption on 23 May. The fit is based on only seven stations in operation at the time. Data from the vertical component at PPX3 are not included in the fits as this component is contaminated by noise. The fits are obtained for a source mechanism consisting of six moment tensor and three single-force components and is representative of the best fit source centroid (Figure 7). Overall, the fits are excellent as demonstrated by the close match between waveforms and small values of residual errors listed in Table 1. Misfits on some components, such as the east component at PPQ2 or north component at PPJ4, may reflect source complexities that cannot be addressed with the single point source used in our analysis.

[26] Although fits based on six moment tensor components yield residual errors that are only a few percent higher than the solution including both moment tensor and force (Table 1), these fits do not represent a physically realistic source mechanism. The resulting moment tensor components display dissimilar waveforms so that no mechanism can be inferred. Fits based on a source consisting of three single-force components only were observed to be far worse than fits obtained for moment and force as demonstrated in the larger residual errors in Table 1. The source model with six moment tensor components and three single-force components consistently yields the minimum value of AIC for this event, indicating that the force components do have significance from a physical viewpoint and that the error reduction is not merely an artifact stemming from an increase in the number of free parameters in the model. This supports our conclusion that this is the most appropriate model to describe the source mechanism of the 23 May eruption. Figure 9 illustrates the source time functions associated with fits depicted in Figure 8. The volumetric components of the moment tensor clearly dominate the solution, with source time functions characterized by almost identical time histories. Accompanying the volumetric source components are two clear components of a single force in the east (x) and vertical (z) directions. The amplitude ratio F_x/M_{xx} is $\sim 0.31 \times 10^{-4}$ m^{-1}, and the amplitude ratio F_z/M_{zz} is $\sim 0.25 \times 10^{-4}$ m^{-1}. Note that for the source-centroid/receiver configuration specific to Popocatépetl our calculations indicate that the single-force and moment tensor components contribute equally to the observed signal amplitudes when this ratio is $\sim 2 \times 10^{-4}$ m^{-1}. Therefore F_x

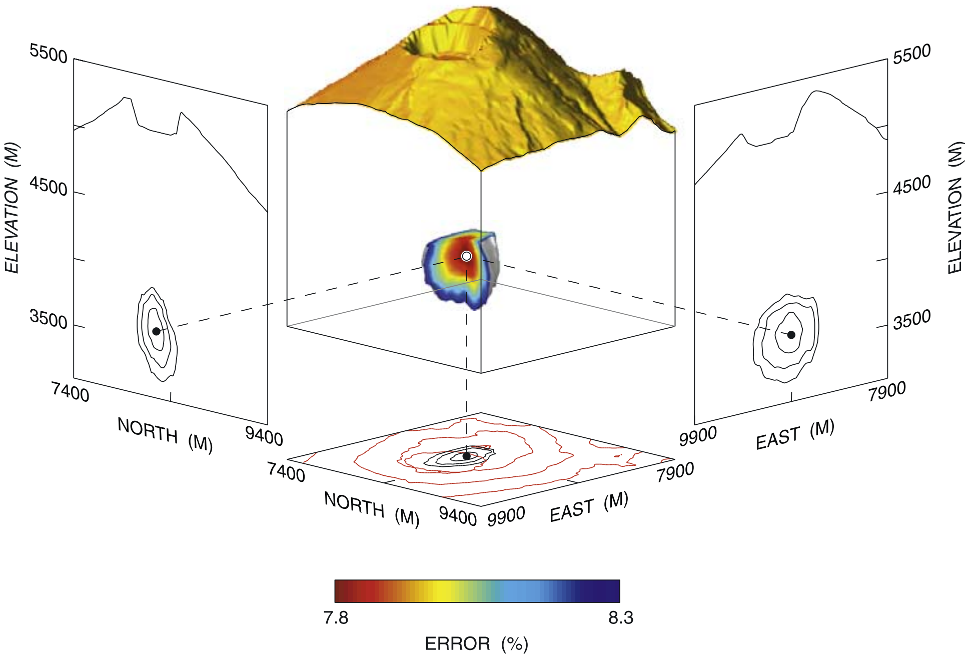

Figure 7. Source location of the 23 May eruption. A southwest looking cutaway view of Popocatépetl provides the reference for the location of the VLP source within the volcanic edifice. The view shows the residual error, color coded according to the magnitude of the error between data and synthetics (see text for details). The gray surface represents the outline of the error region, within which the white dot shows the position of the source centroid corresponding to the minimum error. The side and bottom planes are east-west vertical, north-south vertical, and horizontal cross sections through the source location. Contours on these planes are projections of the error region for the source location. Contours represent 7.9, 8.1, and 8.3% errors. Topographic contours (red lines) in the bottom plane are shown to better picture the source location relative to the summit crater.

contributes up to 16%, and F_z contributes up to 13% of the waveform amplitudes in our solution.

[27] As the waveforms of individual moment tensor components in Figure 9 are consistently shaped, we may obtain a rough estimate of the eigenvectors for these solutions from measurements of the maximum peak-to-trough amplitudes of the source time functions. The principal axes of the moment tensor obtained in this manner have lengths $(1.20, 1.45, 2.00) \times 9.03 \cdot 10^{12}$ Nm with the direction of the dominant dipole component oriented roughly in the *z* direction. The principal axes of the moment tensor for a tensile crack have amplitudes $\lambda\Delta V$, $\lambda\Delta V$, and $(\lambda + 2\mu)\Delta V$, in which ΔV represents the volume change associated with the crack opening or closure, and λ and μ are the Lamé coefficients of the rock matrix [*Chouet*, 1996]. If one assumes a Poisson ratio $\nu = 1/3$ at the source, a value appropriate for volcanic rock at or near liquidus temperatures [*Murase and McBirney*, 1973], the ratios of the principal axes of the moment tensor become 1:1:2. In our solution, the corresponding ratios are not exactly 1:1:2, but rather 1.20:1.45:2.00, suggesting the possibility of a dual mechanism. For example, one can also generate these ratios by the following matrix operation, $(1{:}1{:}2) + 0.4 \times (1{:}2{:}1) = (1.4{:}1.8{:}2.4)$, yielding the ratios (1.17:1.50:2.00) after normalization. This latter result is very close to the observed result of 1.20:1.45:2.00. On the basis of the orientation of the subdominant dipole in our solution, this amounts to adding a 40% contribution from a quasi-vertical crack striking in the northeasterly direction. Therefore our solution is suggestive of two sources acting simultaneously: (1) a shallow dipping crack (sill) and (2) a NE trending quasi-vertical crack (dike). In section 4.5, we test this idea and proceed with a reconstruction of the composite source underlying our solution.

Table 1. Residual Errors E_1 and E_2 Calculated With Equations (6) and (7), Respectively, and Corresponding AIC Calculated With Equation (8) for the Source Mechanisms Considered in Our Inversions of Data for Popocatépetl Volcano[a]

Source Mechanism	Error E_1,[b] %	Error E_2,[b] %	AIC(E_1)	AIC(E_2)
Force only	66.0	52.6	−3199	−5914
Moment only	6.4	12.6	−29355	−21272
Moment and force	4.1	7.8	−33026	−25328
Sill and force	—	46.5	—	−6793
Dike and force	—	18.7	—	−17766
Composite model 1	—	11.8	—	−23309
Composite model 2	—	10.6	—	−24578
Composite model 3	—	9.2	—	−25647
Composite model 4	—	9.5	—	−25341
Composite model 5	—	9.6	—	−25146

[a] Eruption was on 23 May.

[b] Error was estimated over a 2 min long window centered on the window used for waveform inversion.

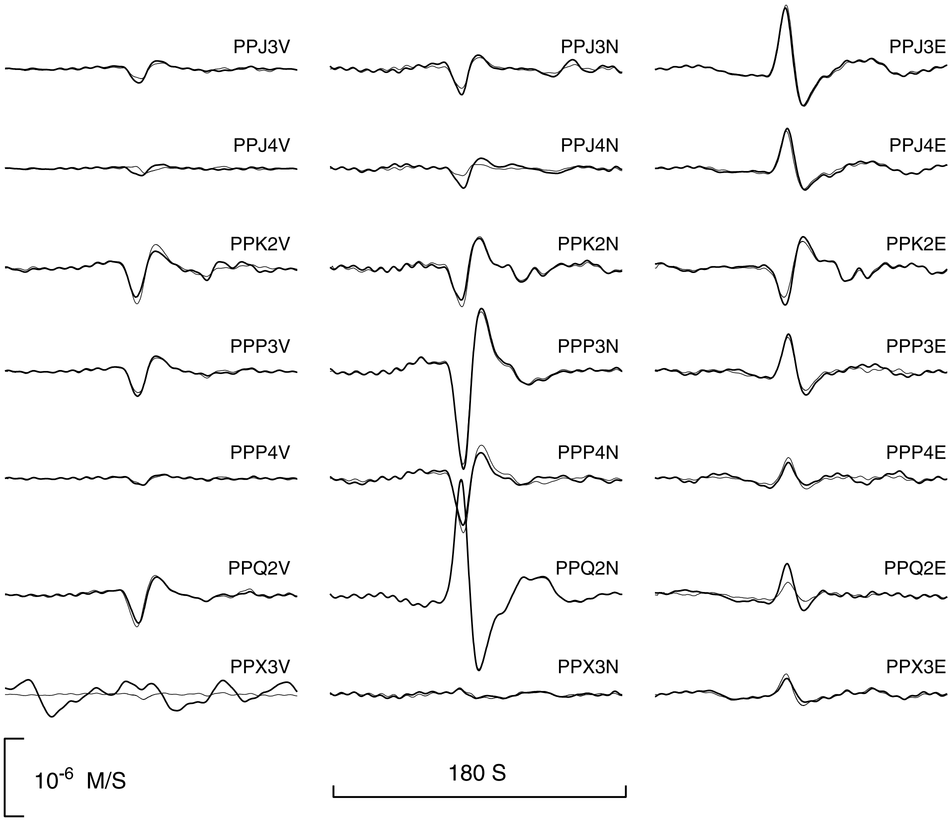

Figure 8. Waveform match obtained for the 23 May eruption, in which six moment tensor and three single-force components are assumed for the source mechanism. Thin lines indicate synthetics, and thick lines represent observed velocity waveforms. The station code and component of motion are indicated at the top right of each seismogram.

4.5. Source Reconstruction

[28] Our hypothesized composite source can be readily tested by (1) calculating the moment tensors for the two cracks using equation (15) of *Chouet* [1996], (2) applying the appropriate scaling factor to the moment tensor representing crack 2, (3) adding the moment tensor for crack 1 to the scaled moment tensor for crack 2, (4) calculating the Green's functions for the resulting moment tensor, and

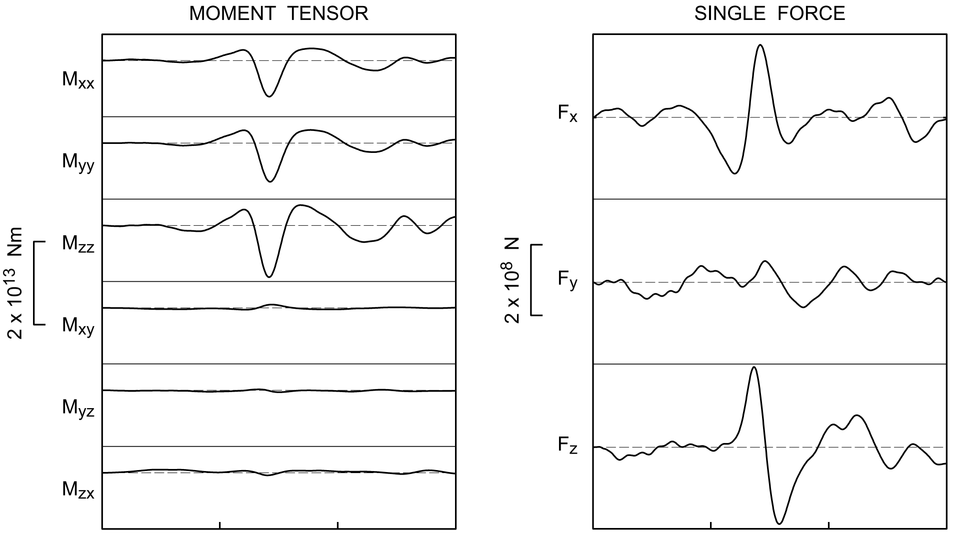

Figure 9. Source time functions obtained for the 23 May eruption, in which six moment tensor components and three single-force components are assumed for the source mechanism.

(5) inverting. In this test, a single source time function applies to both cracks and the orientations of the two cracks are fixed by the directions of the dominant and subdominant dipoles obtained from maximum peak-to-trough measurements of the source time functions of moment tensor components in our original solution. The dipole orientation is given by the azimuth ϕ measured counterclockwise from the east direction, and elevation angle θ measured from the horizontal. The dominant dipole component in our solution has orientation $\phi_1 = -36.85°$, $\theta_1 = 73.57°$, and the subdominant dipole has orientation $\phi_2 = 120.73°$, $\theta_2 = 15.25°$. In our composite model, the orientation of the main dipole component of crack 1 (sill) is given by the angles (ϕ_1, θ_1), and that of the main dipole component of crack 2 (dike) is fixed by the angles (ϕ_2, θ_2).

[29] Our calculations are performed for the point source location in Figure 7, based on the conservative error estimate E_2 in equation (7), and waveform fits obtained with forward models are evaluated from residual errors based exclusively on this equation. As noted earlier, the location of the source centroid obtained according to the definition of error E_1 in equation (6) is different from that of the centroid derived according to E_2. A comparison of residual errors E_1 between forward and original models would therefore require the calculation of a distinct set of models at this location. Such calculations are deemed to be redundant and the following analyses are restricted to the point source solution shown in Figure 7.

[30] Residual errors are evaluated for three models, each including four mechanisms as follows: (1) fixed moment tensor representative of sill (crack 1), together with three single-force components; (2) fixed-moment tensor representative of dike (crack 2), together with three single-force components; and (3) fixed moment tensor representative of composite of sill and dike, together with three single-force components. The sill and force model produces reasonable fits on the east and vertical components in our network, but yields poor fits on the north components. This results in a large residual error of 46.5% (Table 1). The dike and force model yields good fits on the vertical and reasonable fits on the horizontal components, with the exception of the two horizontal components at PPK2 and east component at PPQ2. The resulting error is 18.7% (Table 1). The composite mechanism of dike and sill plus force (composite model 1 in Table 1) yields the best fit of the three models with a residual error of 11.8%. This latter result gives us confidence that a composite mechanism involving both a dike and a sill may be able to explain the results illustrated in Figure 9. The residual error is still too large, however, and even though the number of mechanisms is limited to four in the present model, compared to the nine mechanisms used in our original inversion, examination of the AIC indicates that this simple interpretation falls short of being an appropriate final model for our data.

[31] Next, we evaluate the residual error for a composite model in which the orientations of the two cracks are allowed to vary independently of each other, and the percentage of contribution from crack 2 is also allowed to change. A slightly better fit is obtained for a model in which crack 2 contributes 40% of the observed waveform amplitudes and where crack 1 dips 46° to the southeast and crack 2 dips 52° to the north-northwest. The residual error for this model (composite model 2 in Table 1) is 10.6%. The associated value of AIC, however, suggests that this still is not an adequate model for our data.

[32] To proceed further, we now relax the limitation of our representation of the two cracks by a single source time function and instead allow each crack to be represented by its own source time function. Rather than calculating Green's functions for the moment tensor representing the sum of the moment tensors for crack 1 and crack 2 as done above, we calculate Green's functions for the moment tensor representing each crack mechanism separately, and invert our data for five mechanisms, namely, the two moment tensors representing two independent crack mechanisms, and three single-force components. The resulting moment tensor mechanisms are then combined component by component and the composite mechanism obtained in this manner is compared with the original solution in Figure 9. Our search for a best fitting model is carried out by systematically varying ϕ_1, θ_1, ϕ_2, and θ_2 independently of each other. We consider 22,628 models spanning the ranges [10°, −45°] for ϕ_1, [25°, 90°] for θ_1, [95°, 135°] for ϕ_2, and [5°, 15°] for θ_2. A residual error is calculated for each model and contoured in the four-dimensional space [ϕ_1, θ_1, ϕ_2, θ_2]. We then apply the constraint that the error be limited to values falling within 0.5% of the absolute minimum error.

[33] Figure 10a shows the residual error as a function of ϕ_1, θ_1, and ϕ_2 for $\theta_2 = 7°$. The gray surface represents the surface of residual error 0.5% above the absolute minimum of 9.2% (composite model 3 in Table 1) for the entire model space. The extent of the error domain in this plot provides bounds on the ranges of ϕ_1, θ_1, and ϕ_2, within which the waveform fits are essentially indistinguishable from each other. Horizontal and vertical cross sections through the solution marked by the white dot provide measures of the relative position of this point with respect to the 0.5% error bound above the absolute minimum error. The significance of this particular solution is discussed in detail below. Figure 10b illustrates the sensitivity of the model on θ_2 as expressed by horizontal projections of 0.5% error contours obtained by slicing through the error domain with a slanting plane normal to the $\theta_1 - \phi_2$ plane and containing the point representing the minimum error for each value of θ_2 and point marked by the white dot in Figure 10a. Each contour circumscribes an area within which models satisfy the 0.5% error constraint. The gray shaded contour is representative of the domain shown in Figure 10a. The common area embedded within the overlapping contours includes all the models that satisfy the error constraint for any value of θ_2 within the range [5°, 15°]. A more restrictive condition on θ_2 applies for the solution shown by the solid dot. To fall within the 0.5% error constraint, this model requires $\theta_2 \leq 13°$.

[34] We find the absolute minimum of residual $E_2 = 9.2\%$ for values of $\phi_1 = -20°$, $\theta_1 = 55°$, $\phi_2 = 115°$, and $\theta_2 = 13°$. This solution also yields the minimum AIC (Table 1), suggesting this model may be suitable for our data. There is, however, one additional constraint we need to consider, which has a direct bearing on this result.

[35] So far, we have restricted ourselves to a consideration of residual error and AIC in our search for the optimum model, and have not taken into account the statistical properties of the time-dependent eigenvectors

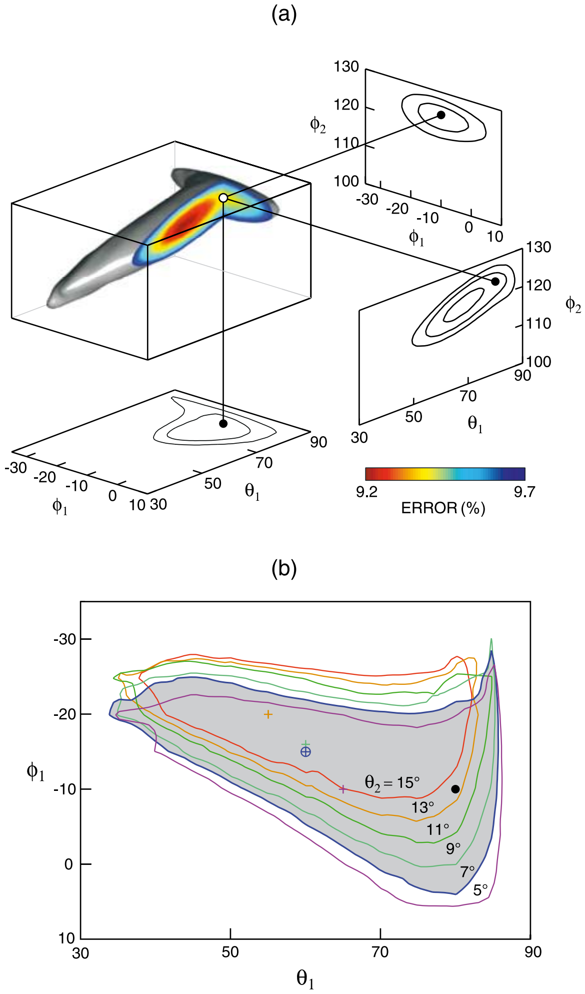

Figure 10. (a) Residual error, color coded according to the magnitude of the error between data and synthetics, for a composite source composed of a shallow dipping crack (sill) intersecting a steeply dipping crack (dike). The gray surface represents the outline of the error region, within which the white dot identifies the solution that matches the statistics of azimuth and elevation angles obtained for the original source model based on six moment tensor and three single-force components (see text for details). The side and bottom planes are cross sections through the point marked by the white dot. Contours on these planes are projections of the error region for these angles. Contours represent 0.3, 0.4, and 0.5% errors (cross section $\theta_1 - \phi_2$) and 0.4 and 0.5% errors (cross sections $\phi_1 - \phi_2$ and $\phi_1 - \theta_1$) above the absolute minimum error of 9.2%. The black dot represents the projection in these planes of the solution fitting the statistics of eigenvectors for the original source. (b) Dependence of the solution in Figure 10a on the elevation angle θ_2. Each contour represents a particular value of θ_2 and is colored accordingly (see contour labels). Black dot is the horizontal projection of the white dot in Figure 10a. Crosses are projections of the points representing the minimum residual error for each displayed value of θ_2. The circled cross represents the minimum error for the contour encompassing the gray shaded area (see text for details).

describing the moment tensor in our original solution (Figure 9). We now consider such statistics in detail to obtain additional constraints on our final model. Figures 11a and 11d show the statistics of the eigenvectors calculated for the moment tensor solution in Figure 9 during the time interval 60–120 s. Figure 11a displays rose diagrams of ϕ_1, ϕ_2, θ_1, and θ_2. Only the dominant and subdominant eigenvectors are depicted in these diagrams as the orientation of the third eigenvector is fixed once the other two are determined. Figure 11d shows histograms of the amplitude ratio of the smallest to largest eigenvector (Figure 11d, left) and amplitude ratio of the subdominant to largest eigenvector (Figure 11d, right), together with the weighted arithmetic mean, $\bar{x}$, of these ratio statistics. The eigenvectors, whose lengths are proportional to their respective eigenvalues, are considered with no distinction between expansion and contraction for simplicity, and the ratios are obtained after normalization to a maximum length of 2.

[36] To compare our model statistics to the statistics in Figures 11a and 11d, we sample the source time functions of the moment tensor in our model of composite source over the same 60–120 s window. A model is retained if the corresponding values of ϕ_1, ϕ_2, θ_1, and θ_2 fall within 5° of the values of these angles in the original model. Out of our entire model set encompassing 22,628 models, only 225 models are found to fit this condition. Figures 11b and 11e show the results obtained by stacking the eigenvector statistics of these 225 models. As is readily apparent in Figures 11b and 11e, there is a good agreement between the overall statistical properties of these models and statistics of our original model. The values of $\bar{x}$ for the eigenvector amplitude ratios in Figure 11e are also very close to those obtained for the histograms in Figure 11d.

[37] The best fitting model with residual error of 9.2% and minimum AIC (composite model 3 in Table 1) is not the optimum model from the perspective of these statistical tests. This particular model contributes a mere 25% of hits within the dominant bins constituting the rose diagrams in Figure 11a. Within the restricted model set displayed in Figure 11b, only two models are found to yield 100% hits in the appropriate bins. Both yield very similar crack orientations. The first of these (composite model 4 in Table 1) yields a residual error of 9.5% and has parameters $\phi_1 = -10°$, $\theta_1 = 80°$, $\phi_2 = 124°$, and $\theta_2 = 7°$. The second (composite model 5 in Table 1) gives a slightly larger residual error of 9.6% with the parameters $\phi_1 = -20°$, $\theta_1 = 80°$, $\phi_2 = 123°$, and $\theta_2 = 8°$. Of these two solutions, model 4 yields a value of AIC marginally smaller than the original AIC (Table 1). This model therefore fits the statistical constraints, minimum AIC requirement, and has a residual error within 0.5% of the minimum residual error obtained for all the forward models. Figures 11c and 11f show the statistics of eigenvectors for this model. These statistics are in good agreement with the main features displayed by the statistics in Figures 11a and 11d. The error corresponding to this model is shown by the white dot in Figure 10a. The horizontal and vertical cross sections in Figures 10a and 10b indicate that this point is well within the 0.5% constraint for which waveform fits become indistinguishable.

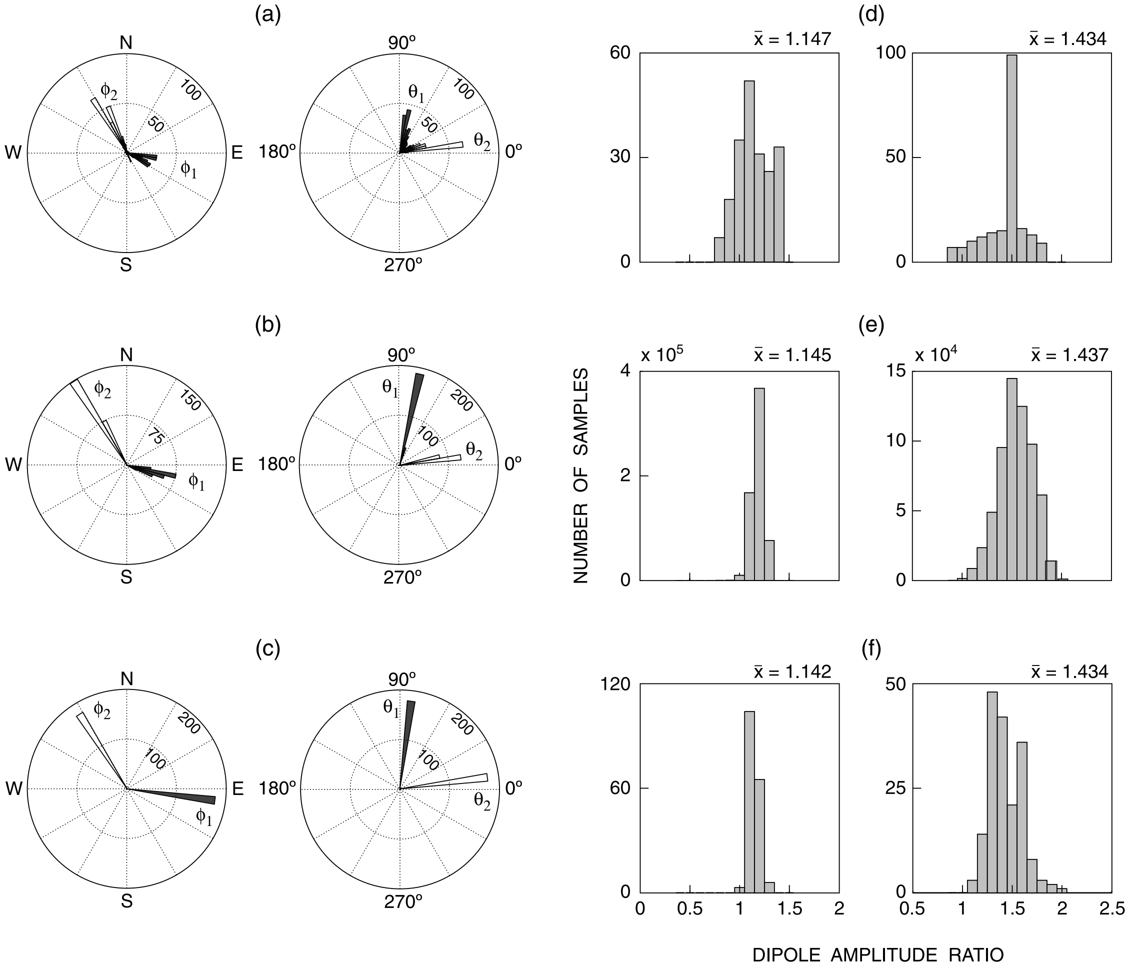

Figure 11. Comparison of eigenvector statistics for the moment tensor in Figure 9 for the solution assuming six moment tensor and three single-force components (Figures 11a and 11d) with those for the moment tensor of a composite source composed of two cracks, each with its own source time function, and three single-force components (Figures 11b, 11c, 11e, and 11f). The eigenvectors are sampled every 0.2 s during the interval 60–120 s in both the original and reconstructed composite source models. (a) Rose diagrams of azimuth ϕ_1 and elevation angle θ_1 defining the orientation of the dominant dipole component of the source (shaded bins) and azimuth ϕ_2 and elevation angle θ_2 defining the orientation of the first subdominant dipole component of the source (open bins). The width of the bin is 5°. (b) Same as Figure 11a obtained by stacking results for 225 models of composite source, whose dominant and subdominant dipole components are oriented within 5° of the corresponding dipole components in the statistics shown in Figure 11a. (c) Same as Figure 11a for the selected composite model, whose dominant and subdominant dipole components yield 100% of hits within the dominant bins for ϕ_1, ϕ_2, θ_1, and θ_2 in Figure 11a. (d) Amplitude ratios of (left) smallest to largest dipole and (right) intermediate to largest dipole after normalization of largest eigenvector to a length of 2. No distinction is made between expansion and contraction. The weighted arithmetic mean $\bar{x}$ is shown at the top right of each panel. (e) Same as Figure 11d for stacked statistics of 225 forward models of composite source. (f) Same as Figure 11d for the selected composite model.

[38] The waveform fits obtained for model 4 are displayed in Figure 12. These fits can be compared with the fits in Figure 8. There are very slight differences between Figures 12 and 8 (compare, for example, the fits obtained on the north component at station PPP3, or east components at PPJ3 and PPJ4). The observed differences are representative of a difference in residual error amounting to 1.7%. Overall, the differences are too small to be noticeable so that the two models may be viewed as equivalent. Figure 13 shows the source mechanism for the composite source, which can be directly compared with the results in Figure 9. As expected, the two sets of source time functions display very similar features. Some nuances are apparent in these results, however. For example, the tail of the source time function of moment components in Figure 13 displays a smoother VLP oscillation compared to the results seen in Figure 9. Also, oscillations with periods 16–24 s are much more apparent in the tail of the signal from the vertical force in Figure 13. Figure 14 shows the source mechanism of the composite source represented by the moment tensor in

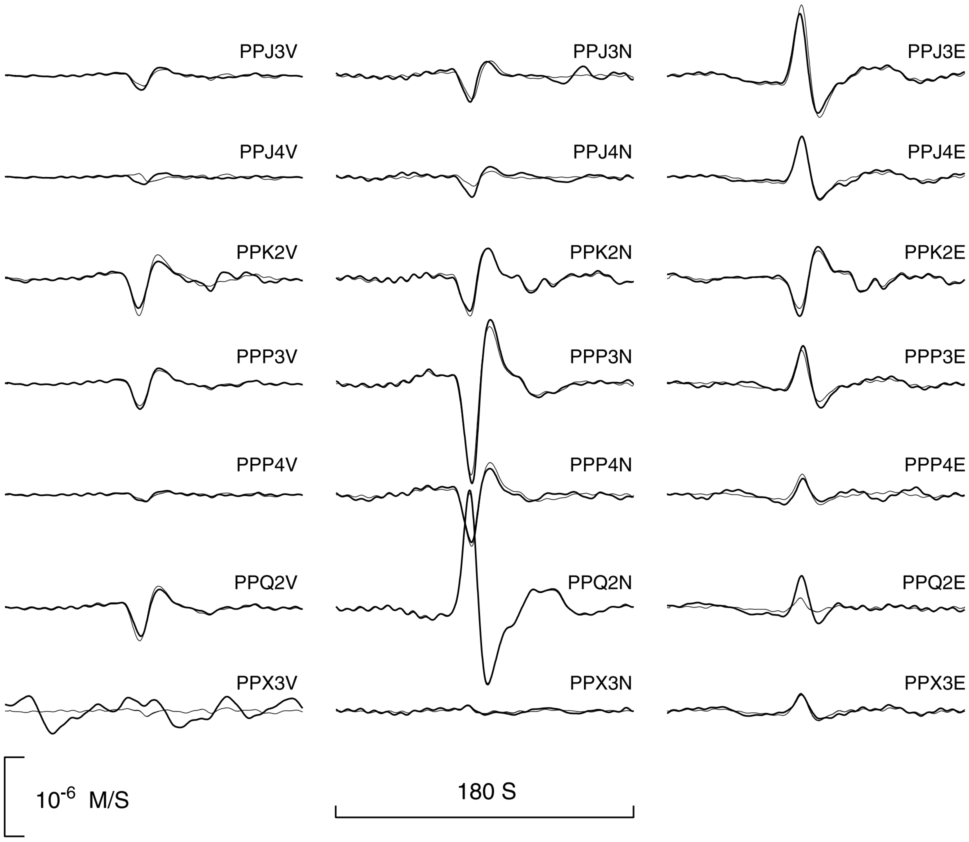

Figure 12. Waveform match obtained from reconstruction of the source mechanism for the 23 May eruption. Thin lines indicate synthetics, and thick lines represent the observed velocity waveforms.

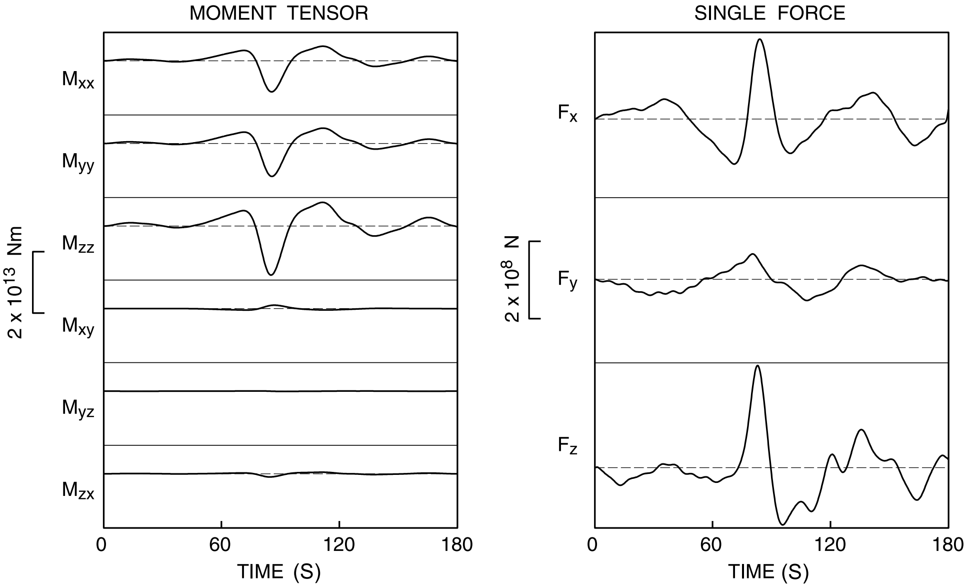

Figure 13. Source time functions of composite source obtained by reconstruction of the source mechanism for the 23 May eruption. The source time function of each moment component represents the sum of the source time functions of corresponding moment components for the dike and sill obtained for the best fitting orientation of these two cracks (see text for details).

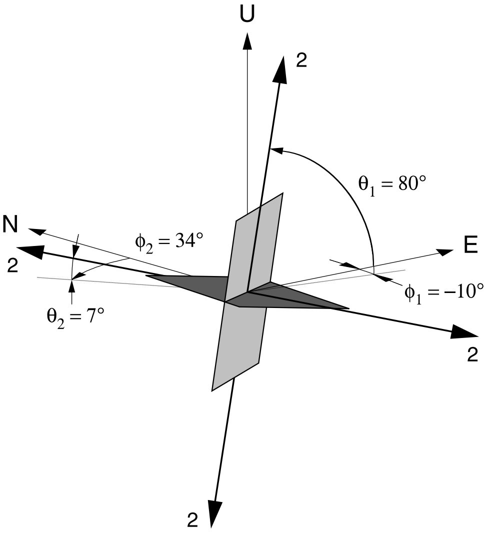

Figure 14. Reconstructed source mechanism for the 23 May eruption. The reference coordinates for the eigenvectors are E (east), N (north), and U (up). Shown are the two dominant dipole components defining the orientations of the dike and sill representing the composite source. The eigenvector statistics for this source are shown in Figures 11c and 11f.

Figure 13. This source mechanism is an adequate representation of the data displayed in Figure 9.

5. Source Process

[39] VLP waveforms associated with the eruption on 23 April were initially inverted using a source mechanism composed of six moment tensor and three single-force components as in the 23 May event. Although the April event was recorded with a larger number of stations compared to the May event (nine stations in April, compared to seven stations in May), the waveforms of the April event contain a stronger component of VLP noise and this approach proved ultimately unsuccessful. No robust mechanism could be extracted from these data owing to distortions in the source time functions obtained for individual moment components. As expected, however, the location of the source centroid for this eruption coincided very closely with that of the May eruption (see Figure 7), strongly suggesting that the same source was operative in April. To test this assumption, we inverted the waveforms of the April event using the composite source elaborated for the May event (composite model 4). Excellent fits, marked by a residual error E_2 = 10.4%, were obtained in that manner, supporting our original assertion that the observed VLP waveforms represent a repetitive activation of the same fixed source.

[40] The volumetric and single-force components of the source processes associated with the eruptions on 23 April and 23 May are shown in Figure 15. Source dynamics are illustrated over a 6 min long window to afford a more complete view of the overall duration of the main component of the VLP process associated with each eruption. The volume changes of the sill and dike are obtained from the amplitude $(\lambda + 2\mu)\Delta V$ of the principal dipole component representing each crack in our composite model. These results assume the value $\mu = 10^{10}$ Pa and Poisson ratio $\nu = 1/3$ $(\lambda = 2\mu)$. For the April eruption, the maximum volume changes are $\Delta V = 1{,}023$ m^3 in the sill, and $\Delta V = 295$ m^3 in the dike. The May eruption shows comparatively smaller maximum volume changes $\Delta V = 522$ m^3 in the sill, and $\Delta V = 169$ m^3 in the dike.

[41] Immediately apparent in Figure 15 are the close dynamic similarities shared by the volumetric sources operative in April and May. Both display an initial inflation of the sill followed by a strong deflation. Sill deflation is followed by a recovery inflation that exceeds the initial inflation. This sequence, which constitutes the dominant component of VLP signal associated with each eruption, is then followed by decaying VLP oscillations lasting several minutes. The signal from the dike is comparatively simpler. In this case, motion is essentially limited to an inflation-deflation-inflation sequence delayed by a few seconds with respect to the main sequence observed in the sill. There appears to be little response from the dike during the decaying oscillations composing the later portions of the volumetric signal from the sill.

[42] Accompanying these volumetric components are significant force components. As discussed by *Takei and Kumazawa* [1994], a single force on the Earth can be generated by an exchange of linear momentum between the source and the rest of the Earth. An upward force can be explained as the reaction force on the Earth associated with either a downward acceleration or upward deceleration of the center of mass of the source volume. Similarly, a downward force may be the result of either an upward acceleration or downward deceleration of the center of mass of the source volume. To facilitate the interpretation of the single-force components in our solution in terms of mass advection, the three components F_x (east), F_y (north), and F_z (up) (e.g., Figure 13) have been recast as in-plane strike and dip components in each crack. Note that the dike plane is tilted 7° from vertical (Figure 14), so that the dip component of force F_{DIP2} is essentially equivalent to the force F_z in Figure 13. Furthermore, the sill plane is slightly tilted along an azimuth 10° south of east, while the dike is striking 34° north of east (Figure 14) so that the force components F_{DIP1} and F_{STRIKE2} share common shapes with the component F_x in Figure 13. The strike of the sill 10° from north also accounts for the close waveform similarities displayed by F_{STRIKE1} in Figure 15 and F_y in Figure 13.

[43] Similarities in the behavior of the force components are apparent in the two eruptions in spite of the larger contribution from noise in the April eruption. The percentage of single-force contribution to the waveform amplitudes is less in the April eruption compared to that in May (F_x and F_z each contribute 8–11% of the waveform amplitudes in the April event compared to 13–16% in the May event). Common behavior is best observed in F_{DIP2}, where both eruptions display a large upward pulse followed by oscillations with periods 16–24 s superimposed on longer-period oscillations with periods in the range 30–70 s. The noisy character of these longer-period oscillations makes a formal identification of their origin doubtful. The shorter-period oscillations, however, clearly start with the upward pulse and decay within an interval of ~1 min, pointing to a

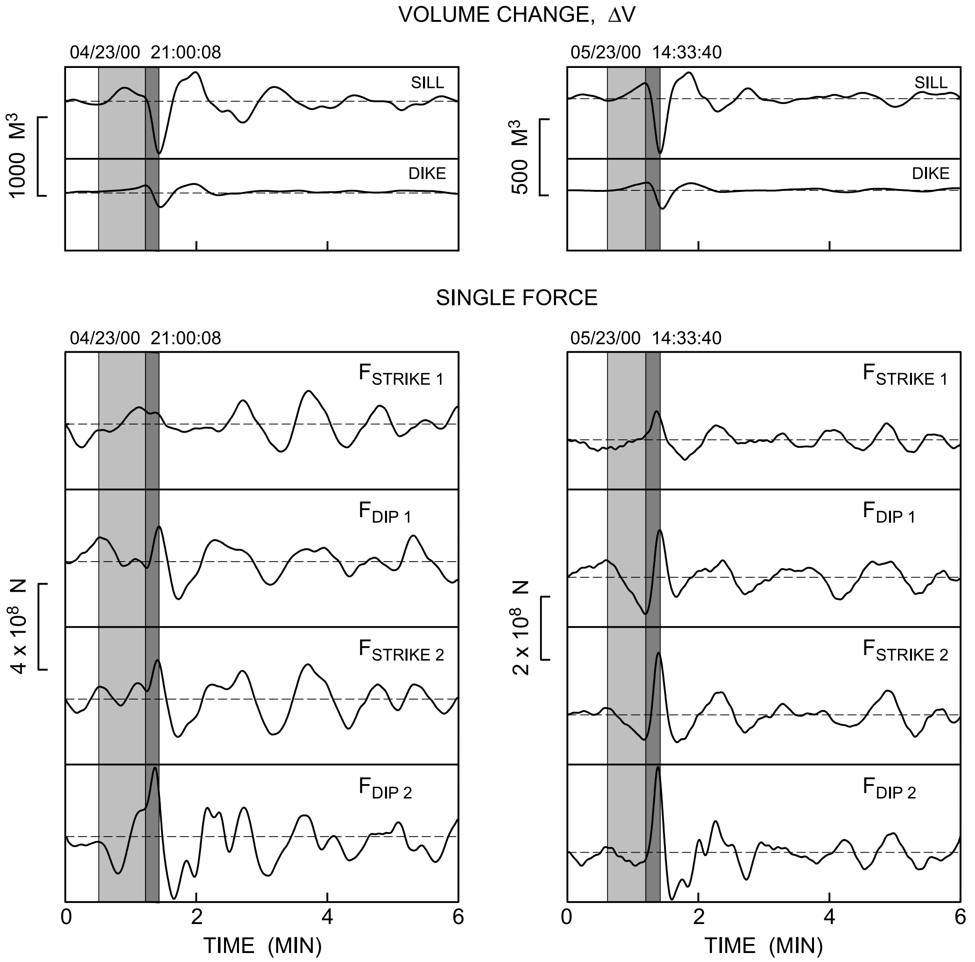

Figure 15. Source time functions of volume change ΔV and in-plane force components in strike (positive along strike measured counterclockwise from east) and dip (positive along dip measured clockwise from the positive strike orientation) directions associated with mass advection in the sill and dike (see source mechanism in Figure 14) for the 23 April and 23 May eruptions. F_{STRIKE1} and F_{DIP1} are the two components in the sill, and F_{STRIKE2} and F_{DIP2} are the two components in the dike. The 6 min long windows are representative of time intervals during which the VLP signals are strongest. Light shading marks the interval during which the initial volumetric inflation of the sill occurs, and dark shading identifies the subsequent interval spanning the dominant deflation phase of the sill. This inflation-deflation sequence is best observed in the May eruption (top right panel) but is somewhat obscured by the presence of VLP noise in the April eruption (top left panel). In the latter the beginning of the interval of dark shading is set to coincide with an abrupt turn in the volumetric signal of the sill.

source origin for these components. Such oscillations are assumed to be related to the dynamics of mass transport.

[44] Most interesting is the behavior of the force components in each crack near the onset of the dominant volumetric signal in the May event (see light shaded interval in Figure 15, right). The initial inflation of the sill coincides with a marked downward (westward) excursion of F_{DIP1} and slightly smaller downward (southwestward) excursion of F_{STRIKE2}. This appears consistent with an eastward acceleration of the center of mass in the sill and slightly smaller northeastward acceleration of the center of mass in the dike. During this time interval, there also appears to be a small downward excursion of F_{DIP2}, which may reflect a slight upward acceleration of the center of mass in the dike. Upon reaching maximum inflation, the sill starts to collapse, followed within seconds by the onset of collapse of the dike (see dark shaded interval in Figure 15, right). During such collapse, the force components all display significant pulses suggesting a strong downward and southwestward acceleration of the center of mass in the dike, and dominantly westward and slightly southward acceleration of the center of mass in the sill. Taken together, these features may be interpreted as the result of an eastward movement of magma originating near the western edge of the sill, occurring synchronously with sill inflation. As magma is squeezed past the dike inlet, magma in the dike inlet is apparently dragged in a northeasterly direction, and a slight uplift of the magma column in the dike is also induced. Following this interval, magma movements in the dike and sill reverse directions and we observe a sagging of the magma column in the dike. The latter impulsive signal is then followed by decaying vertical oscillations of the magma column. Al-

though this behavior of the forces is somewhat obscured by noise for the April eruption, the waveforms within the shaded intervals in Figure 15 (left) point to features that are consistent with this picture.

[45] These results are suggestive of the forced evacuation of a large pocket of gas at or near the western edge of the sill. They further suggest that once the escaping gases reach the dike inlet, gases apparently rush to the surface through preexisting, relatively open pathways. The latter idea is buttressed by the relatively small volume change affecting the dike as compared to the sill. Photographs of the crater taken during quiescent stages show a zone of sustained degassing along the perimeter of the vent, suggesting that the interfacial zone between the magma column and conduit wall may be a predominant pathway used by gases on their way to the surface. Enhanced permeability in this zone may be in the form of a network of fractures resulting from magma fragmentation by viscous shear near the conduit wall during magma ascent [*Gonnermann and Manga*, 2003]. The behavior of the sill associated with degassing is explored below in the specific context of the magma and medium properties anticipated for Popocatépetl.

6. Discussion

[46] Mild ongoing episodic eruptions at Popocatépetl are intimately linked to degassing of a sill-shaped volume of magma through a dike whose surface extension bisects the vent. The volumetric oscillations of the sill (Figure 15) can be interpreted as the result of a series of cyclic pressure fluctuations originating in the magma filling the sill.

[47] Pressure fluctuations associated with repetitive sawtooth waveforms have been observed in laboratory experiments with foams of organic gas-gum rosin mixtures expanding in a vertical tube [*Ryan*, 2001]. These experiments may be particularly relevant to our observations as the gas-liquid flows they investigate were specifically designed to be analogous to those encountered in volcanic conduits. The upgoing ramp in the sawtooth waveform of pressure observed in the laboratory was attributed by *Ryan* [2001] to bubble growth by diffusion from a supersaturated liquid and related pressure increase in the bubbles resulting from the finite yield stress of the overlying foam. At some critical pressure, the yield stress of the overlying foam is overcome and the body of the foam column shears; shear flow then causes the bubbles in the shear zone to coalesce and collapse, thereby providing a temporary pathway for the resulting gas pocket to escape. Pressure in the source region then decreases, and the sheared foam self-heals as stress decreases. This process is repeated until decreasing volatile concentration in the liquid eventually shuts down the diffusion of gas into the bubbles.

[48] In the following, we consider a similar mechanism of diffusion pumping of bubbles in the magma under Popocatépetl, based on the assumption that the magma filling the sill is supersaturated. Magma supersaturation is assumed to be the result of groundmass crystallization in a static body of magma. Diffusion of gas from the melt into bubbles increases the internal pressure of the bubbles, because bubble expansion is resisted by the viscosity of the surrounding liquid and by the confining effect due to the finite yield strength of the overlying column of magma. Elastic inflation of the sill occurs as a result of bubble pressurization, and inflation proceeds until the critical yield strength of the magma column is reached and magma starts flowing out of the sill. Magma fragmentation by viscous shear near the conduit wall may induce the coalescence and collapse of bubbles intersected by shear planes, thereby allowing gas escape through a transient network of fractures. Such dynamics induce a pressure decrease in the sill, which results in the collapse and welding of the fracture network and effectively seals the gas escape route shut. Repeated cycles of shear fracture and welding of magma provide a ratchet mechanism by which the free gas phase in the source region can be recharged and evacuated. The process repeats until equilibrium-saturation conditions are reached, or until obstruction of the gas pathway to the surface leads to an explosive eruption. Field evidence for repeated fracture and healing of magma was recently documented by *Tuffen et al.* [2003] and provides support for such interpretation.

[49] To test our assumption of pressurization by diffusion, we use the model of *Nishimura* [2004]. *Nishimura* [2004] considers the pressure recovery in magma after a sudden pressure drop by taking into account the vesiculation of volatiles in magma. In this model, the magma body is embedded in an infinite, homogeneous, elastic solid. Magma consists of melt including numerous small spherical gas bubbles of identical size. No new bubbles are created and no bubbles are lost during pressure recovery. The gas in the bubbles is assumed to be a perfect gas, and the melt is a compressible liquid saturated with volatiles. Gas density is negligibly small compared to melt density, and gravity and other body forces are neglected. The variables describing magma are melt density, ρ_ℓ, gas density, ρ_g, gas concentration in the melt, C, bubble radius, a, pressure in melt, P_ℓ, gas pressure in bubble, P_g, and volume of magma, V. Subscripts 0 and f identify initial and final values, respectively. For our present purpose, we assume a magma body embedded in a penny-shaped crack initially under uniform confined pressure P_s. Magma is subjected to an initial pressure drop ΔP_0 due to mass withdrawal. The timescale of the pressure drop is assumed to be much shorter than that of the bubble-growth process. Immediately following the pressure drop, pressure in the melt is given by the ambient pressure minus the pressure drop, namely,

$$P_{\ell_0} = P_s - \Delta P_0, \tag{9}$$

while the gas in the bubbles initially remains at pressure

$$P_{g_0} = P_s + \frac{2\sigma}{a_0}, \tag{10}$$

where σ is the surface tension. Bubbles then start to grow by diffusion of volatiles driven by the difference in pressure between the melt and bubbles. After a sufficiently long time, the pressures in the melt and gas reach a static equilibrium condition given by

$$P_{g_f} - P_{\ell_f} = \frac{2\sigma}{a_f}. \tag{11}$$

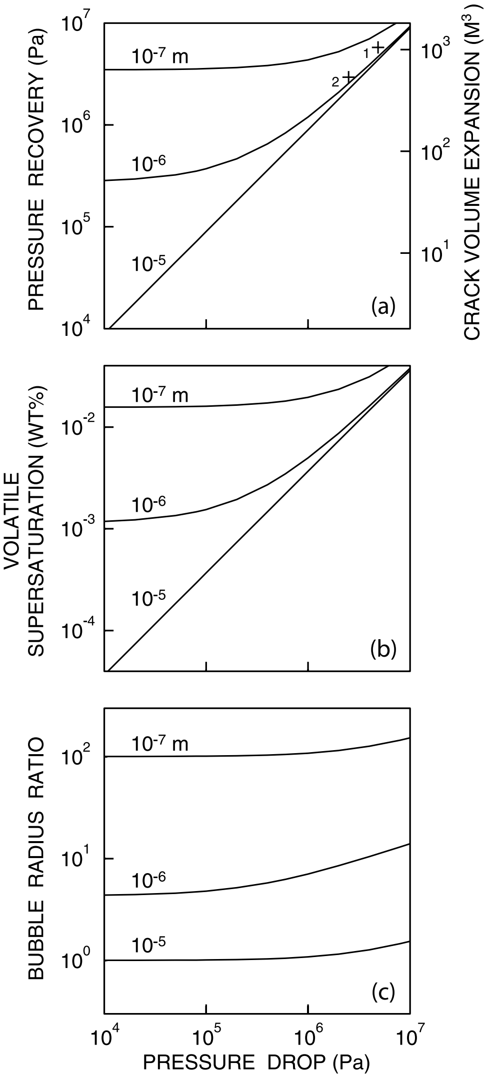

Figure 16. Pressure and volume recovery due to bubble growth driven by diffusion of gas from a supersaturated melt following a degassing-induced pressure drop. (a) Pressure and volume change in a penny-shaped crack containing a bubbly rhyolitic magma, showing effect of different initial bubble radii. The two crosses, numbered 1 and 2, are data for the 23 April and 23 May eruptions, respectively (see text for details). (b) Change in volatile concentration in rhyolitic melt for different initial bubble radii. (c) Bubble growth driven by diffusion of gas from supersaturated rhyolitic melt, showing the effect of different initial bubble radii.

Mass conservation of gas in the magma yields the relation

$$\frac{4}{3}\pi a_f^3 \rho_{g_f} n_g = \rho_{\ell_0}\left(C_0 - C_f\right)\left(1 - \frac{4}{3}\pi a_0^3 n_g\right) + \frac{4}{3}\pi a_0^3 \rho_{g_0} n_g, \quad (12)$$

where n_g is the bubble number density. Volatile concentration in the melt is expressed by Henry's law

$$C_0 = K_H\sqrt{P_{g_0}}\ ; \qquad C_f = K_H\sqrt{P_{g_f}}. \quad (13)$$

Assuming a perfect gas yields

$$\frac{P_{g_0}}{\rho_{g_0}} = \frac{P_{g_f}}{\rho_{g_f}} = \frac{RT}{M}, \quad (14)$$

where R is the universal gas constant (R = 8.314 J/mol/°K), T is temperature (°K), and M is the molecular weight of gas. Pressure in the melt at the completion of the process is related to the volume change of the melt through the bulk modulus of the melt, yielding the relation

$$\Delta P = P_{\ell_f} - P_{\ell_0} = -b\,\frac{\left(\frac{V_f}{V_0} - 1\right) - \frac{4}{3}\pi n_g\left(a_f^3 - a_0^3\right)}{1 - \frac{4}{3}\pi a_0^3 n_g}. \quad (15)$$

For a penny-shaped crack, the excess pressure ΔP is expressed by [*Sneddon and Lowengrub*, 1969]

$$\Delta P = \frac{3}{4}\,\frac{\mu(\lambda + \mu)}{\lambda + 2\mu}\left(\frac{V_f}{V_0} - 1\right)\frac{V_0}{R^3}, \quad (16)$$

where R is the radius of the crack. These equations are solved for unknowns P_{ℓ_0}, P_{ℓ_f}, P_{g_0}, P_{g_f}, ρ_{g_0}, ρ_{g_f}, C_0, C_f, a_f, and V_f, given ΔP_0, P_s, ρ_{ℓ_0}, a_0, n_g, σ, K_H, b, μ, λ, R, and V_0. Volatile concentration in the melt is approximated by using a Henry's law solubility model for water in rhyolitic melt. We use $K_H = 4.33 \times 10^{-6}$ Pa$^{-0.5}$, corresponding to an initial water content of 5.3 wt % at 850°C [*Hurwitz and Navon*, 1994]. Accordingly, we also fix M = 0.018 kg/mole, and T = 1123°K. Melt density is ρ_{ℓ_0} = 2300 kg/m^3 at 5.3 wt % water based on the data of *Hurwitz and Navon* [1994]. We assume $b = 10^{10}$ Pa, $\mu = 10^{10}$ Pa, $\lambda = 2\mu$. The surface tension is σ = 0.2 N/m, based on the experimental results of *Murase and McBirney* [1973] for rhyolite at 850°C.

[50] Our calculations are carried out for a fixed pressure P_s = 40 MPa appropriate for the depth of the source imaged at Popocatépetl. We also assume a fixed radius R = 100 m of penny-shaped crack and account for V_0 through the ratio d/R of crack aperture to crack radius. Figure 16 illustrates results of our calculations. These results are representative of a fixed bubble number density $n_g = 10^{12}$ m^{-3} and fixed crack aspect ratio d/R = 0.05 (a sill 5 m thick), and are plotted as functions of ΔP_0.

[51] Figure 16a shows the pressure recovery ΔP (left scale) and volume expansion $\Delta V = V_f - V_0$ (right scale) during recovery for three initial bubble radii $a_0 = 10^{-5}$ m, $a_0 = 10^{-6}$ m, and $a_0 = 10^{-7}$ m. For small pressure drops, the pressure recovery can be significantly larger than the original drop. This overpressurization upon recovery is largest for tiny bubbles. For example, a pressure drop of $\Delta P_0 = 10^4$ Pa leads to a pressure recovery $\Delta P = 3.5 \times 10^6$ Pa in the presence of bubbles with radii $a_0 = 10^{-7}$ m. The overpressurization decreases with increasing ΔP_0 so that for $\Delta P_0 \simeq 10^7$ Pa the pressure drop is not completely recovered in the presence of bubbles with radii larger than 10^{-6} m.

[52] Figures 16b and 16c show $\Delta C = C_0 - C_f$ and a_f/a_0, respectively, obtained for the same initial bubble radii as in Figure 16a. The net decrease in gas concentration in the melt varies from less than 10^{-4} wt % to more than 10^{-2} wt % over the ranges of bubble radii and pressure drops

depicted. Smaller bubbles grow significantly more than larger bubbles during pressure recovery. This effect is particularly obvious when comparing the ratio a_f/a_0 for tiny bubbles ($a_0 = 10^{-7}$ m) with the same ratio for larger bubbles ($a_0 = 10^{-5}$ m). Overpressurization mainly results from the release of surface tension pressure, so that the magnitude of this effect becomes larger for smaller bubbles. However, overpressurization decreases with increasing ΔP_0, suggesting that the total amount of dissolved volatiles in the melt eventually becomes insufficient to sustain full pressure recovery.

[53] Keeping the same values of R and d as in Figure 16, we investigated the effect of n_b in the range $[10^{10}-10^{14}]$ m^{-3} for a fixed bubble radius $a_0 = 10^{-6}$ m. The results, obtained over the same range of ΔP_0, show a slightly larger pressure recovery for smaller bubble number density, and much smaller pressure recovery for larger bubble number density, for small pressure drops, compared to the results shown in Figure 16. For example, with $\Delta P_0 = 10^4$ Pa, we obtain $\Delta P = 3.5 \times 10^5$ Pa for $n_b = 10^{10}$ m^{-3}, $\Delta P = 2.8 \times 10^5$ Pa for $n_b = 10^{12}$ m^{-3}, and $\Delta P = 1.4 \times 10^4$ Pa for $n_b = 10^{14}$ m^{-3}. The effect of bubble number density decreases with increasing ΔP_0, and becomes trivial when $\Delta P_0 > 4 \times 10^6$ Pa.

[54] The effect of d/R is comparatively minor. A value $d/R < 0.05$ results in a net downward shift of the pressure-recovery curve, while a larger value of d/R has no marked effect on the results displayed in Figure 16a. For $a_0 = 10^{-6}$ m, $n_b = 10^{12}$ m^{-3} and $\Delta P_0 = 10^4$ Pa, we obtain $\Delta P = 2.2 \times 10^5$ Pa for $d/R = 0.01$, and $\Delta P = 2.8 \times 10^5$ Pa for both $d/R = 0.05$ and $d/R = 0.10$.

[55] Values of ΔP predicted by the model may be directly compared to values derived from the source time functions of ΔV in the top panels in Figure 15. Excess pressure is estimated using equation (16), in which we put $\lambda = 2\mu$. This yields $\Delta P = (9\mu/16)(\Delta V/R^3)$. Using $\mu = 10^{10}$ Pa, $R = 100$ m, we obtain $\Delta P = 5.75$ MPa for the maximum volume change in the sill, $\Delta V = 1{,}023$ m^3, in April, and $\Delta P = 2.94$ MPa for the maximum volume change in the sill, $\Delta V = 522$ m^3, in May. From measurements of the peak-to-trough amplitudes of deflation and reinflation in the dominant volumetric signal produced by the sill in Figure 15, we infer the ratio $\Delta P/\Delta P_0 \sim 1.2$ for both the April and May eruptions. Comparing these values of ΔP and $\Delta P/\Delta P_0$ with the results in Figure 16a, we find our data are consistent with those expected for bubbles with radii of $\sim 10^{-6}$ m. A penny-shaped sill with radius 100 m, thickness 5 m, filled with a rhyolitic magma containing $10^{10}-10^{12}$ micrometer-sized bubbles per cubic meter may therefore be an appropriate model for the degassing body at Popocatépetl. Interestingly, the nonlinear response of the bubbly magma to pressure transients seen in Figure 16 may provide a natural way by which small pressure perturbations are magnified. Slow leakage of gases from the magma body may start once a critical threshold is exceeded during quasi-static pressurization of the magma body associated with magma crystallization. Small-scale pressure fluctuations produced by such leakage then may be amplified via the coupling of volatile diffusion and elastic response of the conduit, eventually leading to a surge of degassing as seen in the April and May eruptions. This process of diffusion pumping then repeats itself until the melt becomes undersaturated. Small volumetric oscillations observed prior to the dominant phase of the signals from the sill (Figure 15, top) seem to support the idea of gas leakage as a trigger for these events.

[56] As discussed in section 5, sagging of the magma column may also contribute to the pressure recovery in the sill following the escape of the gas pocket. However, the magnitude $\sim 10^8$ N of the force component F_{DIP2} suggests that this effect is probably quite small. For a dike 5 m thick and 200 m wide, the magnitude of resulting pressure across the cross-sectional area of the dike is $\sim 10^5$ Pa, roughly 10 times smaller than the pressure changes calculated during sill recovery.

7. Conclusions

[57] Inversions of VLP waveforms recorded during two mild eruptions of Popocatépetl Volcano, Mexico, provide an integrated view of the fundamental mechanisms underlying the Vulcanian degassing observed in April–May 2000. The observed VLP waveforms are well fitted by a simple point source located under the western wall of the crater 1,500 m below the crater floor. The imaged source mechanism includes both moment tensor and single-force components. The moment tensor components are representative of a sill with easterly dip of 10° intersecting a northeast striking dike dipping 83° northwest. The surface extension of the dike bisects the vent and this dike is interpreted to represent the main conduit in the top 1.5 km below the summit crater.

[58] The largest moment release occurs in the sill in both eruptions, indicating a maximum volume change of 500–1000 m^3, pressure drop of 3–5 MPa, and amplitude of recovered pressure equal to 1.2 times the amplitude of the pressure drop. In comparison, the maximum volume change in the dike is 200–300 m^3, with a corresponding pressure drop of 1–2 MPa and pressure recovery equal to the pressure drop. Accompanying these volumetric sources is a single force with magnitude of 10^8 N, whose in-plane components in the sill and dike are consistent with melt advection in response to pressure transients. The source time histories of the volumetric components of the source indicate that significant mass movement originates in the sill and triggers a mass movement response in the dike within a few seconds. This picture is consistent with the opening of a pathway for escaping gases accumulated in the sill in response to slow pressurization of the sill driven by magma crystallization. The opening of this pathway and rapid evacuation of pent-up gases induces the pressure drop.

[59] The amplitude of pressure recovery in the sill is much larger than the anticipated pressure variation associated with movement of the magma column perched above the dike in response to the passage of the gas pocket. Rather, pressure recovery in the magma filling the sill is likely to be driven by diffusion of gases from the resulting supersaturated melt into bubbles. Calculations assuming a penny-shaped crack at ambient pressure of 40 MPa suggest that the observed pressure and volume variations may be explained with the following attributes: crack radius (100 m), crack aperture (5 m), bubble number density ($10^{10}-10^{12}$ m^{-3}), initial bubble radius (10^{-6} m), final bubble radius ($\sim 10^{-5}$ m), and net decrease of gas concentration in melt (0.01 wt %). Diffusion pumping is a nonlinear process that displays a sensitive response to small pressure fluctua-

tions. On the basis of this behavior, it seems likely that small pressure variations arising from slow leakage of gases during magma crystallization may eventually lead to a pressure surge and attendant evacuation of a large pocket of gas. Diffusion pumping may remain operative until the source melt becomes undersaturated. Following a sufficiently long lapse of time for magma crystallization to regain melt supersaturation, diffusion pumping may be reinitiated, leading to another eruption. This process may occur repeatedly until either the melt body becomes depleted of gases as it becomes solidified, or the pathway used by the escaping gases becomes clogged up by deposition of hydrothermal minerals [*Stix et al.*, 1997], at which point excess pressurization may lead to an explosive clearing of the pathway.

[60] **Acknowledgments.** We are grateful to D. Escobedo, F. Lizarraga, H. Lopez-Loera, and C. Valdes from the Instituto de Geofisica, Universidad Nacional Autónoma de Mexico (UNAM); G. Espitia, F. Galicia, E. Guevara, and R. Quass from the Centro Nacional de Prevención de Desastres (CENAPRED); G. Asch and R. Kind from the GeoForschungZentrum (GFZ) in Potsdam; P. Chouet and C. Dietel from the U.S. Geological Survey (USGS); M. Galicia from the Protección Civil Amecameca Edo de Mexico; and D. Arenas, M. Galicia, and his rescue team for their participation in the field experiment. We are indebted to David Hill and Robert Tilling of USGS for thorough reviews and helpful suggestions. We also thank Hiroyuki Kumagai, an anonymous reviewer, and the Associate Editor of JGR for constructive comments.

References

Akaike, H. (1974), A new look at the statistical model identification, *IEEE Trans. Autom. Control.*, *AC-9*, 716–723.

Aki, K., and P. G. Richards (1980), *Quantitative Seismology*, 932 pp., W. H. Freeman, New York.

Arciniega-Ceballos, A., B. A. Chouet, and P. Dawson (1999), Very long-period signals associated with Vulcanian explosions at Popocatépetl Volcano, Mexico, *Geophys. Res. Lett.*, *26*, 3013–3016.

Arciniega-Ceballos, A., C. Valdes-Gonzalez, and P. Dawson (2000), Temporal and spectral characteristics of seismicity observed at Popocatépetl Volcano, central Mexico, *J. Volcanol. Geotherm. Res.*, *102*, 207–216.

Arciniega-Ceballos, A., B. Chouet, and P. Dawson (2003), Long-period events and tremor at Popocatépetl Volcano (1994–2000) and their broadband characteristics, *Bull. Volcanol.*, *65*, 124–135.

Aster, R., S. Mah, P. Kyle, W. McIntosh, N. Dunbar, J. Johnson, M. Ruiz, and S. McNamara (2003), Very long period oscillations of Mount Erebus Volcano, *J. Geophys. Res.*, *108*(B11), 2522, doi:10.1029/2002JB002101.

Chouet, B. (1996), New methods and future trends in seismological volcano monitoring, in *Monitoring and Mitigation of Volcano Hazards*, edited by R. Scarpa and R. I. Tilling, pp. 23–97, Springer, New York.

Chouet, B., G. Saccorotti, P. Dawson, M. Martini, R. Scarpa, G. De Luca, G. Milana, and M. Cattaneo (1999), Broadband measurements of the sources of explosions at Stromboli Volcano, Italy, *Geophys. Res. Lett.*, *26*, 1937–1940.

Chouet, B., P. Dawson, T. Ohminato, M. Martini, G. Saccorotti, F. Giudicepietro, G. De Luca, G. Milana, and R. Scarpa (2003), Source mechanisms of explosions at Stromboli Volcano, Italy, determined from moment tensor inversions of very-long-period data, *J. Geophys. Res.*, *108*(B1), 2019, doi:10.1029/2002JB001919.

Comité Cientifico Asesor CENAPRED-UNAM (1995), *Volcán Popocatépetl Estudios Realizados Durante la Crisis de 1994–1995*, 339 pp., Centro Nac. de Prev. de Desastres, Mexico City.

Cruz-Atienza, V. M., J. F. Pacheco, S. K. Singh, N. M. Shapiro, C. Valdés, and A. Iglesias (2001), Size of Popocatépetl volcano explosions (1997–2001) from waveform inversion, *Geophys. Res. Lett.*, *28*, 4027–4030.

Dawson, P. B., C. Dietel, B. A. Chouet, K. Honma, T. Ohminato, and P. Okubo (1998), A digitally telemetered broadband seismic network at Kilauea Volcano, Hawaii, *U. S. Geol. Surv. Open File Rep., 98-108*, 121 pp.

Goff, F., et al. (1998), Geochemical surveillance of magmatic volatiles at Popocatépetl volcano, México, *Bull. Geol. Soc. Am.*, *110*, 695–710.

Gonnermann, H. M., and M. Manga (2003), Explosive volcanism may not be an inevitable consequence of magma fragmentation, *Nature*, *426*, 432–435.

Hidayat, D., B. Chouet, B. Voight, P. Dawson, and A. Ratdomopurbo (2002), Source mechanism of very-long-period signals accompanying dome growth activity at Merapi volcano, Indonesia, *Geophys. Res. Lett.*, *29*(23), 2118, doi:10.1029/2002GL015013. (Correction to "Source mechanism of very-long-period signals accompanying dome growth activity at Merapi Volcano, Indonesia", *Geophys. Res. Lett.*, *30*, 1502, doi:10.1029/2003GL017211, 2003.)

Hill, D. P., P. Dawson, M. J. S. Johnston, A. M. Pitt, G. Biasi, and K. Smith (2002), Very-long-period volcanic earthquakes beneath Mammoth Mountain, California, *Geophys. Res. Lett.*, *29*(10), 1370, doi:10.1029/2002GL014833.

Hurwitz, S., and O. Navon (1994), Bubble nucleation in rhyolitic melts: Experiments at high pressure, temperature and water content, *Earth Planet. Sci. Lett.*, *122*, 267–280.

Kaneshima, S., et al. (1996), Mechanism of phreatic eruptions at Aso Volcano inferred from near-field broadband seismic observations, *Science*, *273*, 642–645.

Kawakatsu, H., T. Ohminato, H. Ito, and Y. Kuwahara (1992), Broadband seismic observation at Sakurajima Volcano, Japan, *Geophys. Res. Lett.*, *19*, 1959–1962.

Kawakatsu, H., T. Ohminato, and H. Ito (1994), 10-s-period volcanic tremors observed over a wide area in southwestern Japan, *Geophys. Res. Lett.*, *21*, 1963–1966.

Kawakatsu, H., S. Kaneshima, H. Matsubayashi, T. Ohminato, Y. Sudo, T. Tsutsui, K. Uhira, H. Yamasato, H. Ito, and D. Legrand (2000), Aso94: Aso seismic observation with broadband instruments, *J. Volcanol. Geotherm. Res.*, *101*, 129–154.

Kumagai, H., T. Ohminato, M. Nakano, M. Ooi, A. Kubo, H. Inoue, and J. Oikawa (2001), Very-long-period seismic signals and caldera formation at Miyake Island, Japan, *Science*, *293*, 687–690.

Legrand, D., S. Kaneshima, and H. Kawakatsu (2000), Moment tensor analysis of near-field broadband waveforms observed at Aso Volcano, Japan, *J. Volcanol. Geotherm. Res.*, *101*, 155–169.

Love, S. P., F. Goff, D. Counce, C. Siebe, and H. Delgado (1998), Quantitative passive infrared spectroscopy of the eruption plume at Popocatépetl volcano, México, *Nature*, *396*, 563–567.

Macias, J. L., G. Carrasco, H. Delgado, A. L. Martin, C. Siebe, R. Hoblitt, M. F. Sheridan, and R. I. Tilling (1995), Mapa de Peligros del Volcán Popocatépetl: Mapa e informe técnico al Comité Cientifico Asesor de la Secretaria de Gobernación, map with explanation booklet, 14 pp., Cent. Nac. de Preven. de Disastres, Univ. Nac. Autonoma de México, Mexico City.

Murase, T., and A. R. McBirney (1973), Properties of some common igneous rocks and their melts at high temperatures, *Geol. Soc. Am. Bull.*, *84*, 3563–3592.

Neuberg, J., R. Luckett, M. Ripepe, and T. Braun (1994), Highlights from a seismic broadband array on Stromboli Volcano, *Geophys. Res. Lett.*, *21*, 749–752.

Nishimura, T. (2004), Pressure recovery in magma due to bubble growth, *Geophys. Res. Lett.*, *31*, L12613, doi:10.1029/2004GL019810.

Nishimura, T., H. Nakamichi, S. Tanaka, M. Sato, T. Kobayashi, S. Ueki, H. Hamaguchi, M. Ohtake, and H. Sato (2000), Source process of very long period seismic events associated with the 1998 activity of Iwate Volcano, northeastern Japan, *J. Geophys. Res.*, *105*, 19,135–19,147.

Ohminato, T., and B. A. Chouet (1997), A free-surface boundary condition for including 3D topography in the finite difference method, *Bull. Seismol. Soc. Am.*, *87*, 494–515.

Ohminato, T., and D. Ereditato (1997), Broadband seismic observations at Satsuma-Iwojima Volcano, Japan, *Geophys. Res. Lett.*, *24*, 2845–2848.

Ohminato, T., B. A. Chouet, P. B. Dawson, and S. Kedar (1998), Waveform inversion of very-long-period impulsive signals associated with magmatic injection beneath Kilauea volcano, Hawaii, *J. Geophys. Res.*, *103*, 23,839–23,862.

Rowe, C. A., R. C. Aster, P. R. Kyle, J. W. Schlue, and R. R. Dibble (1998), Broadband recording of Strombolian explosions and associated very-long-period seismic signals on Mount Erebus Volcano, Ross Island, Antarctica, *Geophys. Res. Lett.*, *25*, 2297–2300.

Ryan, G. A. (2001), The flow of rapidly decompressed gum rosin di-ethyl ether and implications for volcanic eruption mechanisms, Ph.D. thesis, 461 pp., Lancaster Univ., Lancaster, U. K.

Siebe, C., and J. L. Macias (2004), Volcanic hazards in the Mexico City metropolitan area from eruptions at Popocatépetl, Nevado de Toluca, and Jocotitlán stratovolcanoes and monogenetic scoria cones in the Sierra Chichinautzin Volcanic Field: Field Guide, paper presented at Penrose Conference on Neogene-Quaternary Continental Margin Volcanism, Geol. Soc. of Am., Metepec, Mexico, Jan.

Siebe, C., M. Abrams, J. L. Macias, and J. Obenholzner (1996), Repeated volcanic disasters in Prehispanic time at Popocatépetl, central Mexico: Past key to future?, *Geology*, *24*, 399–402.

Sneddon, I. N., and M. Lowengrub (1969), *Crack Problems in the Classical Theory of Elasticity*, 221 pp., John Wiley, Hoboken, N. J.

Stix, J., R. C. Torres, L. M. Narváez, G. P. J. Cortés, J. A. Raigosa, D. M. Gómez, and R. Castonguay (1997), A model of Vulcanian eruptions at Galeras Volcano, Colombia, *J. Volcan. Geotherm. Res.*, *77*, 285–303.

Takei, Y., and M. Kumazawa (1994), Why have the single force and torque been excluded from seismic source models?, *Geophys. J. Int.*, *118*, 20–30.

Tameguri, T., M. Iguchi, and K. Ishihara (2002), Mechanism of explosive eruptions from moment tensor analyses of explosion earthquakes at Sakurajima Volcano, Japan, *Bull. Volcanol. Soc. Jpn.*, *47*, 197–215.

Tuffen, H., D. B. Dingwell, and H. Pinkerton (2003), Repeated fracture and healing of silicic magma generates flow banding and earthquakes?, *Geology*, *31*, 1089–1092.

Uhira, K., and M. Takeo (1994), The source of explosion eruptions at Sakurajima volcano, Japan, *J. Geophys. Res.*, *99*, 17,775–17,789.

Valdes, C., G. Gonzalez, A. Arciniega, E. Nava, and M. Santoyo (1995), Sismicidad del Volcán Popocatépetl a partir del 21 de Diciembre de 1994 al 30 de Marzo de 1995, in *Volcán Popocatépetl: Estudios Realizados Durante la Crisis de 1994–1995*, pp. 129–138, Comité Cient. Asesor CENAPRED-UNAM, Mexico City.

A. Arciniega-Ceballos, Instituto de Geofisica, Universidad Nacional Autónoma México, México City, Mexico.

B. Chouet and P. Dawson, U. S. Geological Survey, 345 Middlefield Road, MS 910, Menlo Park, CA 94025, USA. (chouet@usgs.gov; dawson@usgs.gov)